2011

Computed Tomography Reconstruction: Investigating the Effect of Varying Circle Diameter

William F. Sanders IV
Wright State University

Computed Tomography Reconstruction: Investigating the Effect of Varying Circle Diameter

A thesis submitted in partial fulfillment
of the requirements for the degree of
Master of Science

By:

William F. Sanders IV
B.S. United States Air Force Academy, 2003

2011
Wright State University

WRIGHT STATE UNIVERSITY

SCHOOL OF GRADUATE STUDIES

9 June 2011

I HEREBY RECOMMEND THAT THE THESIS PREPARED UNDER MY SUPERVISION
BY William F. Sanders IV ENTITLED Computed Tomography Reconstruction: Investigating the Effect of Varying Circle Diameter BE ACCEPTED IN PARTIAL FULFILLMENT OF THE REQUIREMENTS FOR THE DEGREE OF Master of Science

_____
Brent D. Foy, Ph.D.
Thesis Director

_____
Lok C. Lew Yan Voon, Ph.D.
Chair, Department of Physics

Committee on
Final Examination

_____
Brent D. Foy, Ph.D.

_____
Gary C. Farlow, Ph.D.

_____
Douglas Petkie, Ph.D.

_____
Andrew Hsu, Ph.D.
Dean, Graduate School

ABSTRACT

Sanders IV, William F. M.S. Department of Physics, Wright State University, 2011. Computed Tomography Reconstruction: Investigating the Effect of Varying Circle Diameter.

In Computed Tomography (CT) reconstruction, several methods for determining the intensity of individual pixels from the back-projection of the scanned profiles exist. The standard reconstruction method uses linear interpolation between ray values to determine pixel intensity. This study quantifies the effects of varying circle diameter on the accuracy of an alternative method where the pixel is approximated as a circle and the area contributions calculated.

A library of 104 scans in 3 image families was created by a synthetic CT scanner and reconstructed with circle radii from 0.1 to 1.0 pixel in 0.1 pixel steps. Images were compared against a baseline and accuracy measured. Image quality was poor and measures erratic for radii smaller than 0.5 pixels where it stabilized. The overall optimum of the radius was determined to be 0.5 pixels for all images. The reconstructed image quality was not a significant improvement over the standard linear interpolation method.

TABLE OF CONTENTS

LIST OF FIGURES

LIST OF TABLES

ACKNOWLEDGEMENT

I would like to acknowledge Dr. Thomas N. Hangartner Ph.D., Distinguished Professor & Director of the Biomedical Imaging Laboratory, for giving me the basics of CT and the idea for this study in his CT class and Dr. Brent Foy Ph.D., Associate Professor of Physics, for guiding the idea through completion. I like to recognize the sacrifice of my family while I worked during the evenings and late into the night writing the software that made this study possible and their love and support to see me through to completion.

INTRODUCTION

Computed Tomography, better known as CAT or CT, has transformed the ability of medical professionals to diagnose and treat internal abnormalities and injuries. Similarly it has allowed a broad expanse of non-destructive testing to improve industrial quality control, preventative diagnostics, and failure analysis (Buzug, 2008). This revolutionary technique was the result of combining modern computing power with classical mathematical methods in the recombination of radiographic projections taken from multiple angles through a target medium. These projections are filtered to reduce the geometric effects of the scan and noise then reassembled into a 2D cross-sectional image of the radiometric density of the target medium.

When using the most common reconstruction method, the linear interpolation method, intensity values are assigned to the pixel by use of a proximity weighting basis where the projection ray values contribute to the pixel in proportion to their proximity to the pixel center (Peters, 1981). Normally only the two closest rays to the center of the pixel are considered and the centerline of the detector element the rays are used for distance calculations. This technique is relatively computationally simple and allows for edge information shared between rays to contribute to an edge pixel. However the ray's contribution to the pixel value is not tied to the percentage of area that the ray covers so the contributed amount can vary by rotational angle.

The Circle Area Weighted technique explored here focuses on an alternative method of assigning the intensity values to individual pixels. In this method the pixel is approximated as a circle and the ray boundary passing through the circle determines the contribution of each ray to the pixel intensity. The circle size can be varied to include or exclude overlap between pixels for ray contribution. One possible disadvantage of this approach is that the approximation of the pixel as a circle is not geometrically accurate since physical pixels are square. This can lead to dead spaces in the corners of the pixels for small circle sizes and overlap as the circle radius passes 0.5 pixels with continued dead spots in the corners till the radius exceed 0.7 pixels. This method of reconstruction does not appear to have been studied before in published literature.

In this study we will evaluate circle diameter reconstruction as compared to a MatLab built in 'iradon' method using linear interpolation reconstruction with identical filtering (Mathworks, Inc, 2004). To evaluate the methods, three images were used as synthetic phantoms to simulate medical, industrial, and maximum entropy images. Factors such as edge location and definition as well as density accuracy were explored.

BACKGROUND AND THEORY

CT History and Scan Generation: Sir Godfrey Hounsfield and Allen Cormack shared the Nobel Prize for Medicine in 1979 for this pioneering work ***(The Nobel Assembly of Karolinska Institutet, 1979)***. The foundation of any CT scanner is the ability to create discreet "rays" through the target medium which represent the cumulative radiodensity, stored as an intensity pixel, along the path of the X-rays from source to the detector.

The intensity pixel representing each ray are combined to form projections that are a linear array, or B-scan, of the radiodensities along the linear travel of the source and detector across the target volume. By rotating the source/detector around the target volume a series of projections is made that represent the B-scans of the target as viewed from discrete angles as demonstrated in Figure 1.

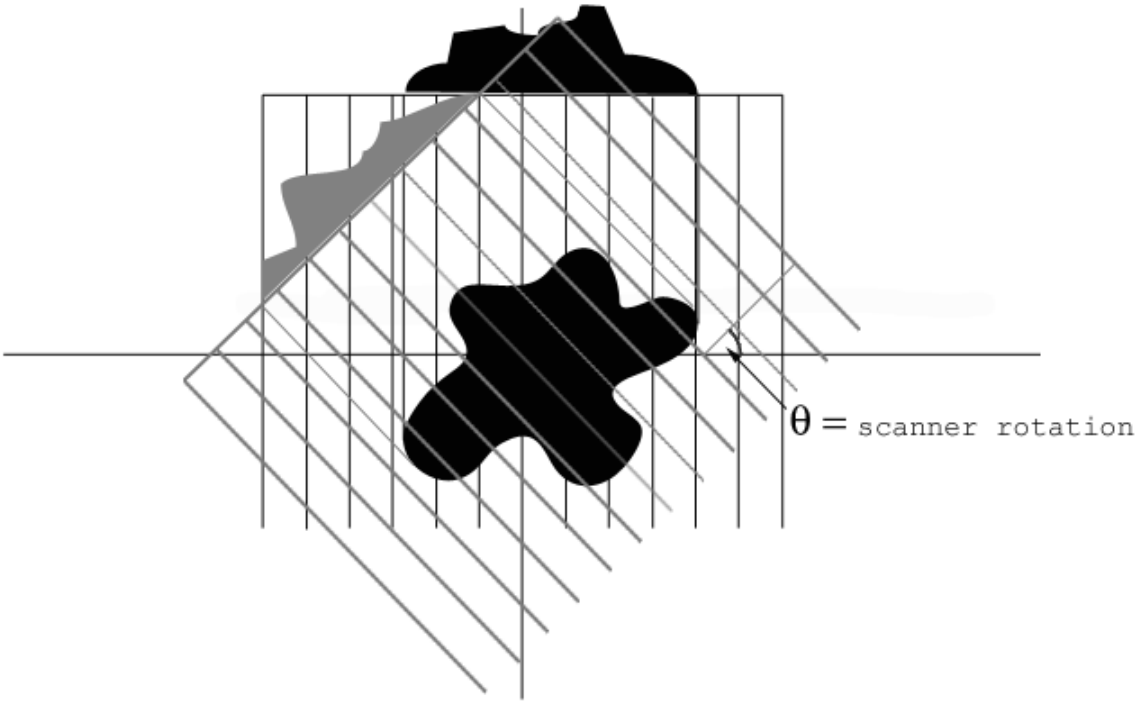

Figure 1. B-scan profiles of radon (cumulative radiodensity) rays through a target medium at 0 and θ angles.

The collection of these B-scan projections forms the basis of a 2D slice of the radio-density of the target medium. Through various reconstruction methods the B-scan projections can be recombined into a 2D image of the radio-density of the target.

Early scanners were limited by the computing power of the day and the physical methodology of the scanners in their ability to acquire a scan and then reconstruct the image. The original EMI head scanner used the 1st generation scan methodology of translate-rotate, where the source and detector translated linearly along the full width of the projection then rotated before acquiring the next projection as seen in Figure 2.

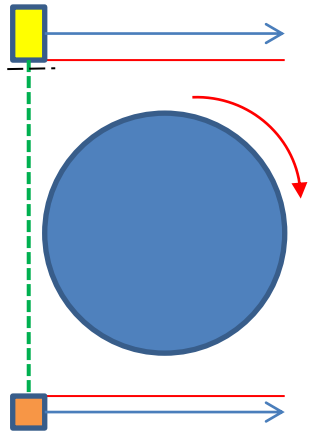

Figure 2. 1st Generation pencil beam "translate-rotate CT Scanner system as used by Hounsfield.

The earliest reconstruction methods relied on the inverse radon transform of the B-scan projections to recreate the target image (Goldman, 2007). The inverse radon transform required the entire scan to be completed before any reconstruction could begin. This was due to the need to filter the entire slice worth of projections together using a Fourier Transform and/or other filtering before the reconstruction could begin. With the limitations of computing power of the day, this lead to very long lag times after the scan before the image could be produced for analysis and any follow up scans taken. The original EMI scanner took a full 2.5 hours to reconstruct a scan of the head (Beckman, 2006).

Subsequent 2nd generation scanner systems refined the physical methodology to speed up the scan time by employing multiple detectors, reducing the number of linear translation steps required per angle (Goldman, 2007).

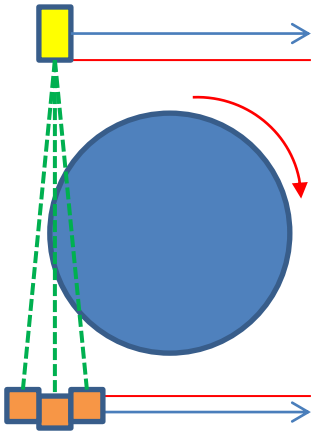

Figure 3. 2nd Generation “Fan-Beam, Translate-Rotate” CT scanner

This created fan beam projections instead of the translate-rotate parallel beam geometry. The introduction of multiple detectors introduces the problem of beam scatter causing inaccurate contributions to detectors outside of the geometric beam path. To combat this collimators are installed between detectors but the physical thickness of the collimator causes dead spots between pixels, reducing spacial resolution. 3rd generation scanners uses a single source and curved detector array for continuous scanning without the need for linear translation (Goldman, 2007). However the source and detector array still rotate around the target medium.

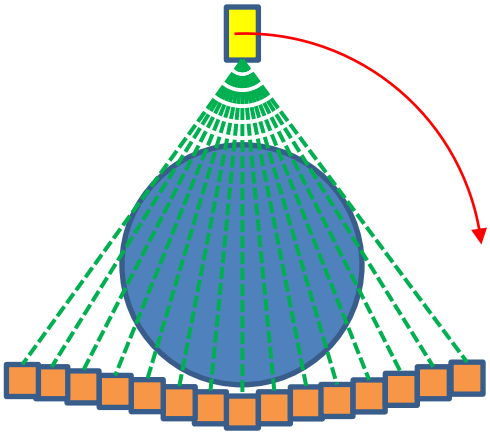

-

Figure 4. 3rd Generation "Fan-Beam" rotate only CT scanner with a the entire target medium enclosed in the fan beam.

The most modern single slice 4th generation scanners replace the rotating detector array with a continuous 360º array and use software to control the activation of required detectors (Goldman, 2007).

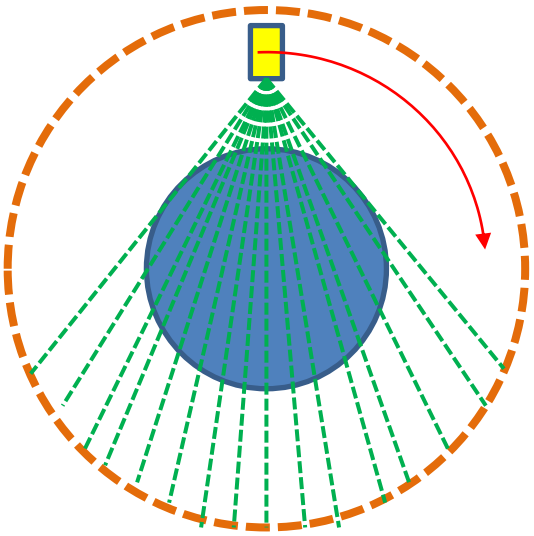

Figure 5. 4th Generation 360º detector fan beam CT scanner where the source rotates inside of the detector ring.

Further generations of CT scanners expanded the technology to 3D imaging with the use of multiple rows of detectors to stack 2D B-scan slices generated from a cone beam on top of each other to form a 3D C-scan of the target medium and spiral CT where the source and detectors, or the target medium, move in a helical pattern along the Z-axis (Goldman, 2007). All fan and cone beam scanners rely on the concept of "parallel rearrangement" to create the needed pair of parallel rays through the target medium, essentially converting the data back into parallel beam projections. Spiral CT breaks from this and interpolates the missing rays between the known ray values to complete the data set needed for reconstruction.

Reconstruction Methods: Individual pixels of a reconstruction represent the radiodensity at each pixel as an intensity value where 0 represents full transmission, 0 density such as air, and 1 represents 0 transmission where the X-ray beam is completely absorbed by the target medium. Often it is desired to extract the physical properties of the target medium from the reconstruction; intensity values are used in conjunction with known energy dependent radio densities of objects in the image, such as air and/or water, to calculate the density in a dimensionless value of Hounsfield Units. This conversion allows for standardized comparison of materials across machines and calibration against standards ***(Buzug, 2008)***.

The mathematical basis of reconstructing a CT image is the Fourier Slice Theorem and Radon Transform (Buzug, 2008). These formulas describe dissolving an image, or other 2D profile, into discrete characteristic projections and then reassembling the projections back into the original via an inverse transform. Mathematically the Fourier Slice Theorem uses Fourier transforms from specific angles to dissolve the image which could then be reassembled using inverse Fourier transforms along each angle. However when imaging a physical object, the internal make up is not known so there is no function or other source of data to Fourier transform. However the Radon transform utilizes line integrals through an object or image which can be considered to be no more than the mathematical expression for the cumulative radiodensity along an X-ray beam path through an object. As implimented in the context of CT, the reconstruction of the individual radiodensity path values into an image is known as backprojection, the most

basic of which is the linear backprojection and proceeding in complexity up to filtered fan/cone beam backprojection (Buzug, 2008).

As with the generation of raw projection data, reconstruction methods also take measures to decrease the time requirements with the creation of the convolution backprojection which uses a predefined map or map of functions known as a kernel, of the size of the reconstructed image to correct for the geometric effects of the scan and reconstruction. Because the convolution is predefined, the image can be reconstructed while the scan is ongoing, resulting in the final image being ready far quicker. However convolution backprojection also requires all filtering parameters to be incorporated into the map or kernel at creation. Bulk Fourier Transform based filtering cannot be done on an image until it is reconstructed.

The overall the impact of the fan and cone beam scanners and convolution backprojection was to increase scanner speed, which correspondingly decreased patient dose, and decrease reconstruction time (Buzug, 2008). The trade offs in spatial resolution and filtering abilities were considered acceptable in the light of the medical need to limit dose and increase patient throughput on the very expensive machines. While industrial imaging largely does not suffer from dose limitations, process throughput was still a very important factor in justifying the cost of the process. While the scanner generations define the physical method of ray and projection collection, any reconstruction method can be applied if the slice data is stored.

Regardless of the filtering methodology, the task of reconstructing data from a continuous medium onto a finite matrix of pixels requires the utilization of different approximations of how the data from each ray contributes to an individual pixel. Like the scanners and reconstruction techniques, there was a progression of the approximations used to apply these values to the pixels. The 0^{th} order approximation method was to simply apply the value from the closest ray centerline to the pixel.

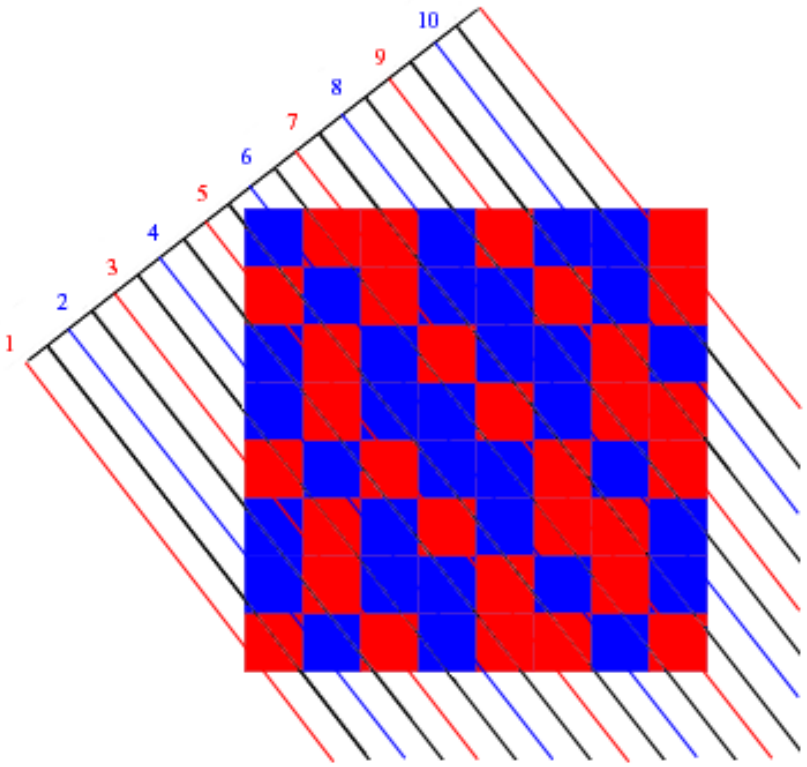

Figure 6. Diagram of 0^{th} order nearest neighbor approximation pixel intensity assignment where the pixel is assigned the value of the closest ray to the center of pixel.

While simple, this approximation was largely inaccurate as structures would lose their detail with pixels being assigned intensities from a single ray when their value more accurately lay on a continuum between adjacent ray values (Lewitt, Bates, & Peters, 1978). An attempt to address this short coming was made with the 1st order linear interpolation approximation. In this approximation, the distance of centerline of the ray (detector) to the center of the pixel was inversely proportional to the ray's contribution to the pixel value. This approximation could be applied using a single ray or multiple rays in a weighting scheme to give an average value to a pixel from the surrounding rays.

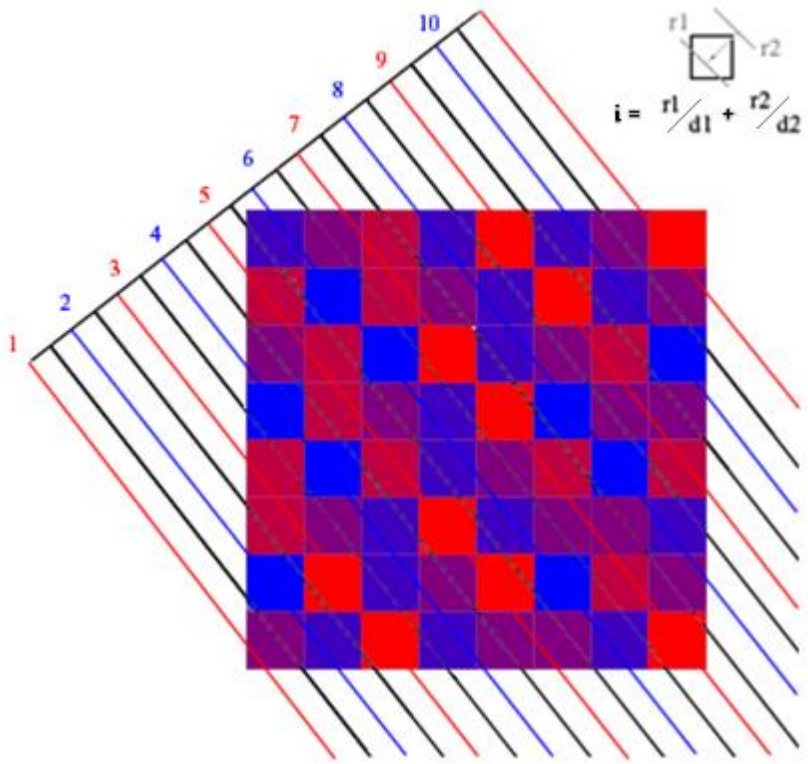

Figure 7. Diagram of 1st order linear interpolation pixel intensity assignment where the intensity value i is determined by the weighted factors inversely proportional to the distance d*n* to the detector centerline r*n*.

The draw back was once again the value of the pixel is based on the distance of the ray centerline to the pixel center determining the importance, not the actual percentage of the area of the pixel covered by a particular ray. However for most applications this technique is sufficient to generate images of acceptable accuracy and reduced computational requirements (Peters, 1981). As a result, this technique is the most commonly used in commercial scanners.

The 2nd order approximation addressed the area function by treating the pixel as a square and calculating the percentage of the area covered by a particular ray. This is the most dimensionally accurate way to reconstruct the image since the rays are overlaid over the exact territory they scanned. The disadvantage of the square is that it requires the calculation of the angle and resultant triangular and/or irregular pentagonal sections of the area which is very computationally complex and time consuming.

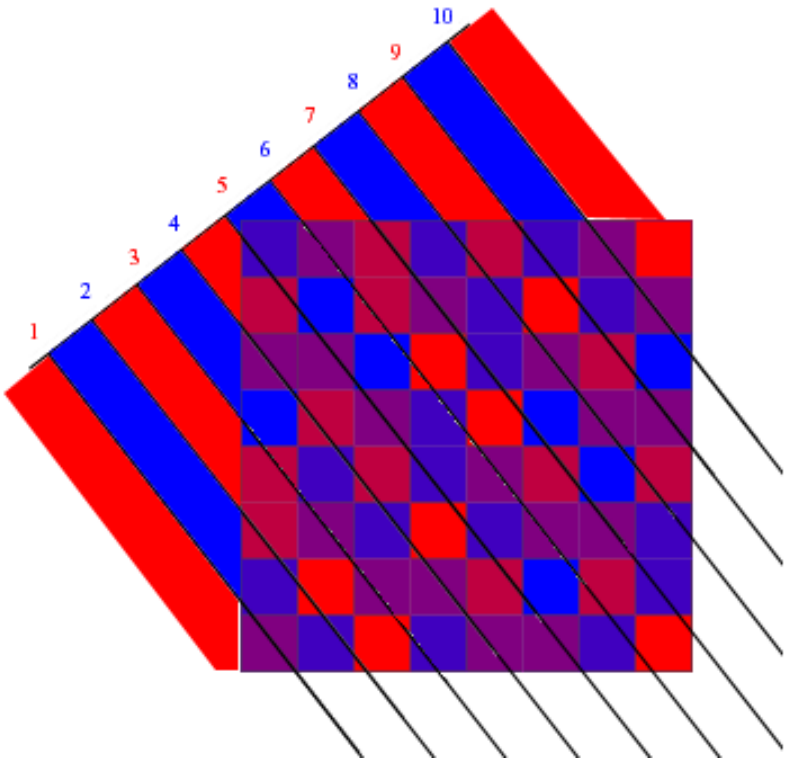

Figure 8. Diagram of 2nd order area weighting approximation pixel intensity assignment showing pixel intensity as a function of area inside of a particular ray.

METHODS

Software: The generation of synthetic scans, both reconstruction algorithms, and the data analysis used MatLab software. The scan generation, 'radon', and the linear interpolation reconstruction, 'iradon', method used algorithms that were already available in MatLab. The circle-weighted reconstruction and the data analysis routines were constructed during the execution of the project

Phantom images: Product literature from various medical CT devices determined the maximum image size while lower end sizes were extrapolated to fit the possibility of industrial scanner with very large object capacity but limited detector quantities ***(GE Healthcare, 2008)***. Similarly, scanner rotation step size covers a realistic range of parameters useful both to medical and industrial imaging.

Three different images were used as phantoms for the analysis series. The first was a "Shepp-Logan" phantom, Figure 9a., generated out of MatLab's 'phantom' function of the desired image size. The phantom itself is a rough simulation of a head containing a 1 (full density) ring representative of the skull surrounding various internal structures imbedded in a 0.2 density field which simulates brain matter. There are internal voids for nasal sinus simulation and overlapping structures of 0.3 density values; the overlapping regions plus up to 0.4 for two structures and down to 0.1 for a structure and void (Shepp

& Logan, 1974). While not a recognized standard, the "Shepp-Logan" is widely known and used in simulation of tomographic reconstruction. The second and third phantoms were created especially for the study. The second image used was a model of the Olympic rings, Figure 9b., with each ring having a progressively higher density (0-0.5) with summing intersection increasing the density range. This image was created to simulate a complex industrial part with multiple interior voids. The final image set was a random distribution of 0-0.4 Gaussian noise of 0.n values that had been subjected to a one pixel 'imdilate' command to expand the points into 3x3 diamond shaped points to allow the analysis tools to work on them, Figure 9c. Unlike the previous two images, the random nature of the Gaussian noise dictated that each image size be different from any other image of the same family. However since the images were intended to analyze the effectiveness of the reconstruction algorithm on an extremely varied image with very small structures, maximum entropy, the overall objective was achieved. The Noise phantom is also unique because it is continuous to within a few pixels of the circle that could be scanned by a physical CT system. Both the "Shepp-Logan" and Ring phantom fit within the same circle but do not have the noticeable limits like the Noise phantom does. The three phantom images can be seen in Figure 9.

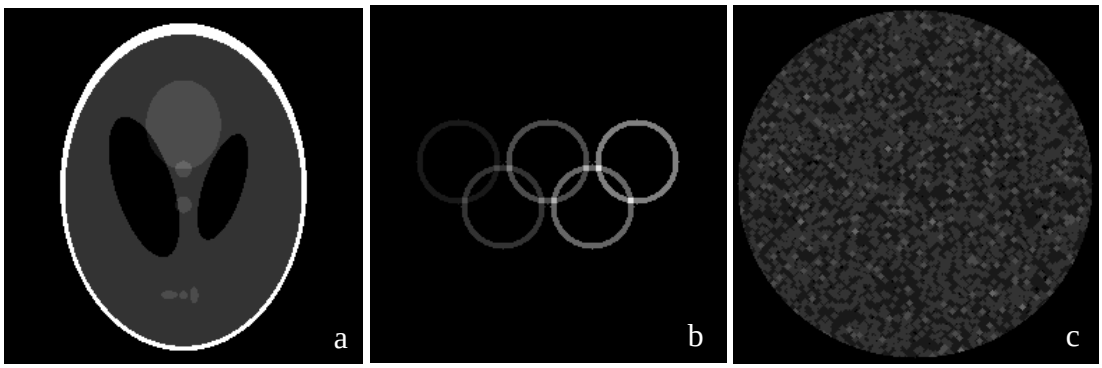

Figure 9. a."Shepp-Logan", b.Ring, and c.Noise phantom images of 256x256 pixel image size.

For each of these images a square phantom of 128-512 pixels in 64 pixel steps was generated. These base images were scanned using a synthetic scanner in 2º-5º rotational step sizes with corresponding 180-72 projections per scan.

Synthetic scan generation: A scratch built scanner utilizing the Bresenham 3D digital line approximation algorithm was constructed (Pendelton, 1992). The scanner first symmetrically zero padded the image out to roughly double size then rotated the end points of the Bresenham line around the target image. The line was then used as the coordinate system to extract and sum the pixels of the target image for each ray. Since the Bresenham line approaches its minimum length at approximately 45º, all points were normalized to the average density along the line to remove the line length variation from the scan. However this process was extremely slow and took over 6 min to complete the most intensive scan since it was the digital analog of the 1st generation translate-rotate scanner. After comparison with the built in 'radon' function, the built in 'radon' function produced nearly identical scans while requiring only ~20s for the most intensive scan, so it was selected for faster phantom generation time. Both the scratch built and the 'radon'

functions produced scans containing a B-scan along each column and rows representing the individual ray cumulative radiodensity (detector intensity). The resulting transform of the "Shepp-Logan" phantom is shown in Figure 6.

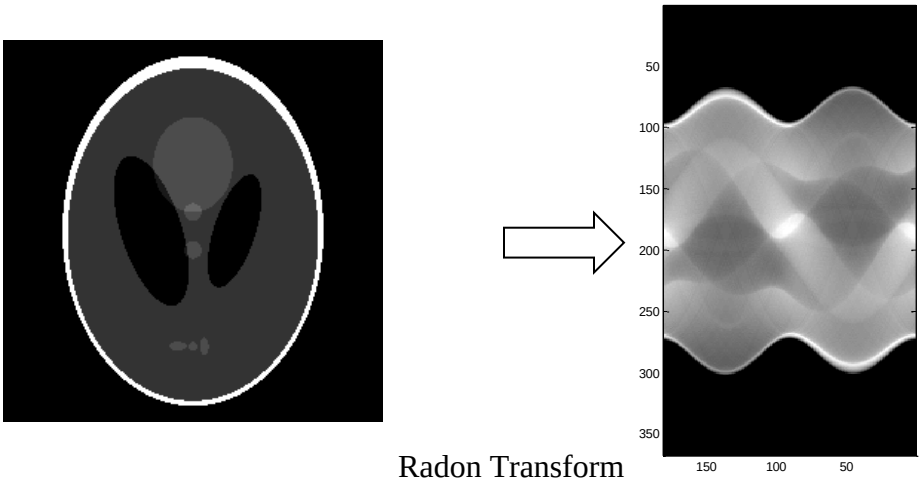

Figure 10. Radon transform of a 256x256 pixel "Shepp-Logan" phantom image with 180 rotational steps corresponding to a 2º rotational step size.

Oversized synthetic scan generation: Since physical matter is not composed of discrete points; using an image much larger than the synthetic detector quantity allows each detector point to represent a physical beam through the target by compressing a scan into a "standard" sized scan matrix (128x128-512x512 pixel matrixes). To approximate a scan of a continuous medium, an image of much larger dimensions than the detector width was chosen. The image is first zero padded to a square since any physical scan would take place inside of a full width circle inscribed in a square space. Since the transform only generates sums along given rays, the zero padding has no effect on the scan. The image dimension is divided by 64 and the integer result used as the base image size. Images larger than 512x512 after square padding use 512 as the base image size. 512x512 proved to be the maximum size the reconstruction map generator could handle

due to memory limitations. Consulting product documentation for various medical CT systems revealed the maximum size of a current reconstruction matrix is 512x512 pixels so this reconstruction limit is consistent with current system maximum capabilities. The image is again zero padded out to the next multiple of the base image size and centered within the field. For images that have a non-symmetric padding split, the lower (coordinate wise) side takes the smaller while the upper takes the larger padding. After conventional scanning using the 'radon' function, the scan is compressed down to "standard" scan matrix dimensions by averaging all the pixels within a range defined by the multiplication factor of the base image into a single scan pixel. While this does affect the reconstructed size of the object, it allows the synthetic scanner to realistically create scans without any approximations to compress the scan down to a standard and reconstructable size. This compression also mimics physical detector behavior where the sum of the different line paths from a source to a detector of physical width through the target medium. Since the intensity stored for each ray can be considered a percent of attenuation, the averaging of the rays for compression is an accurate representation of the compression vs. summing. This size change is somewhat noticeable in Figure 11 where a 1490x1490 pixel "Shepp-Logan" phantom has been compressed after scan then reconstructed into a 512x512 pixel image.

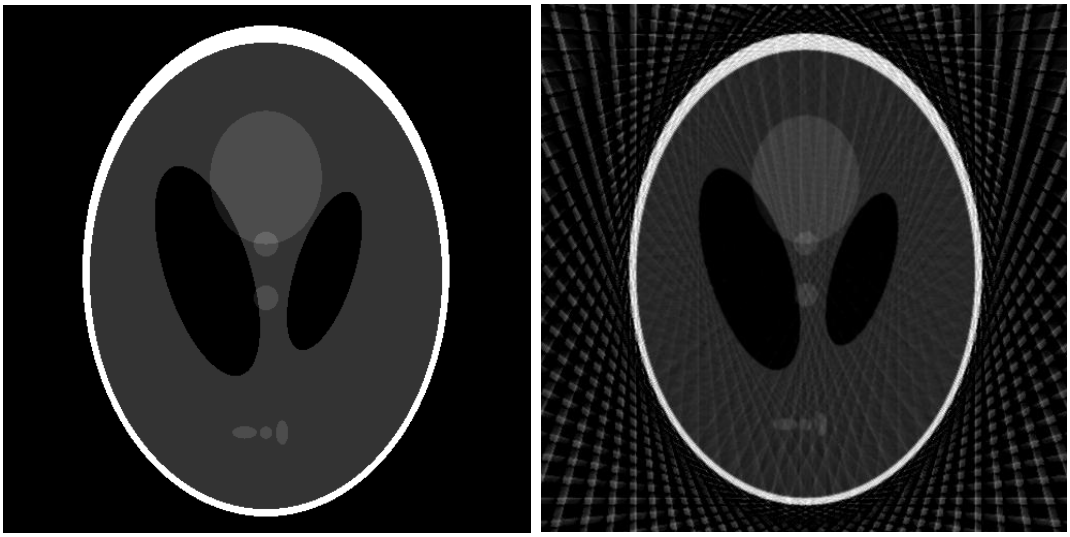

Figure 11. 1490x1490 pixel "Shepp-Logan" phantom (resized for space) with 512x512-5º and 0.6 pixel radius reconstruction of the same image showing relative size shift of the reconstructed image.

Experimental 3rd Order Reconstruction: An alternative reconstruction technique used in this research is to approximate the pixel as a circle centered at the middle of the pixel. This "3rd" order circle weighting approximation has the advantage mathematically that any line through a circle is identical to any other line crossing at the same distance from the origin ***(Ruegesegger, et al., 1980)***.

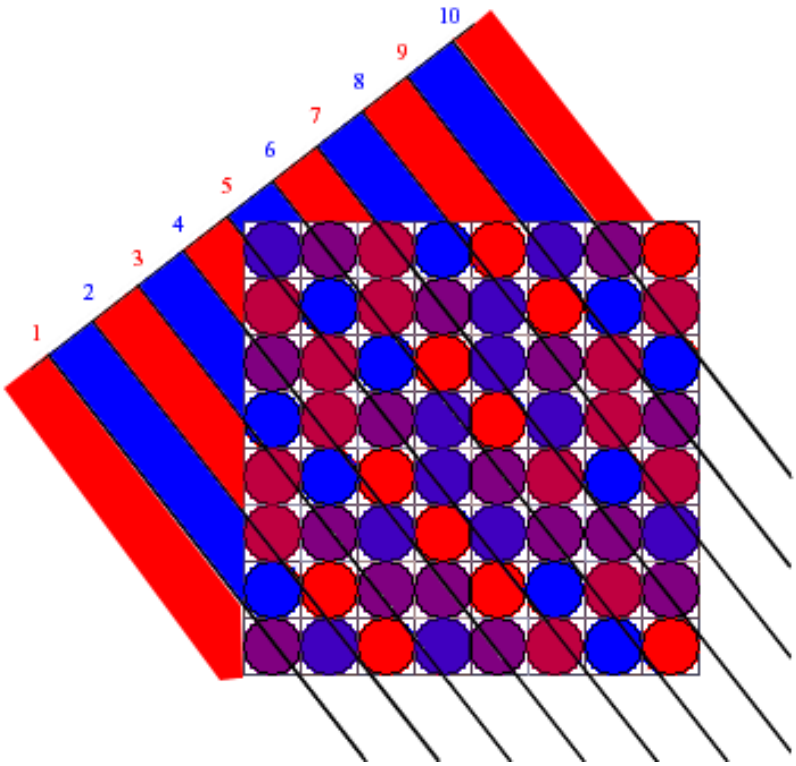

Figure 12. Diagram of 3rd order area weighting approximation pixel intensity assignment showing pixel intensity as a function of area inside of a particular ray.

The other advantage of the circle is that the perimeter is equidistant from the origin and therefore the ability of a ray boundary to pass through the area is not dependent on the projection angle. The disadvantage of the circle approximation is that the pixels are physically square and a circle of equal area will not cover the same physical space as the square pixel leading to dead spots and/or overlapping areas of contribution between pixels illustrated in Figure 13.

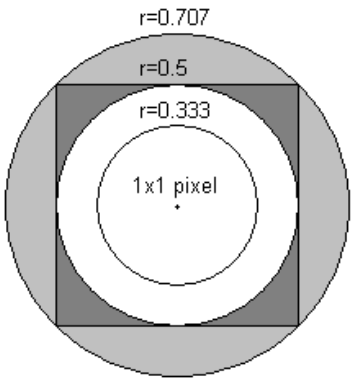

Figure 13. 1x1 unit pixel with overlaid circle approximations showing dead areas and overlaps based on circle radius.

Reconstruction Methodology: Any ray can be defined in Cartesian coordinates by a line in slope-intercept form as shown in Eq. 1.

$$y = -\frac{a}{b}x - \frac{c}{b} \tag{1}$$

From this line the minimum distance to any other Cartesian point (m, n) can be calculated via Eq. 2 where d is the distance.

$$d = \frac{|a \cdot m + b \cdot n + c|}{\sqrt{a^2 + b^2}} \tag{2}$$

Because of scanner rotation, coordinates for each ray is defined in a local Cartesian coordinate system of r, s defined in relation to the x, y plane by Eq. 3 and shown graphically in Figure 14, where θ is the angle of the scanner.

$$\begin{aligned} r &= x \cdot \cos\theta + y \cdot \sin\theta \\ s &= -x \cdot \sin\theta + y \cdot \cos\theta \end{aligned} \tag{3}$$

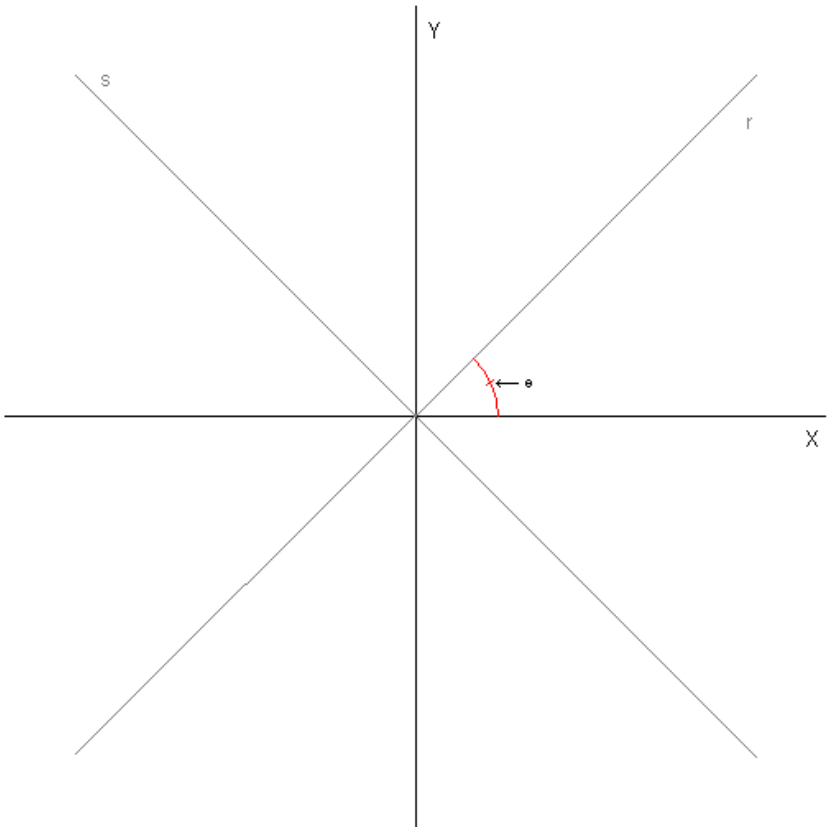

Figure 14. x-y to r-s coordinate system relationship through the angle θ.

The linear representation of the detector array is a straight line along the local s axis at the gantry radius so all rays are defined by a vertical r line.

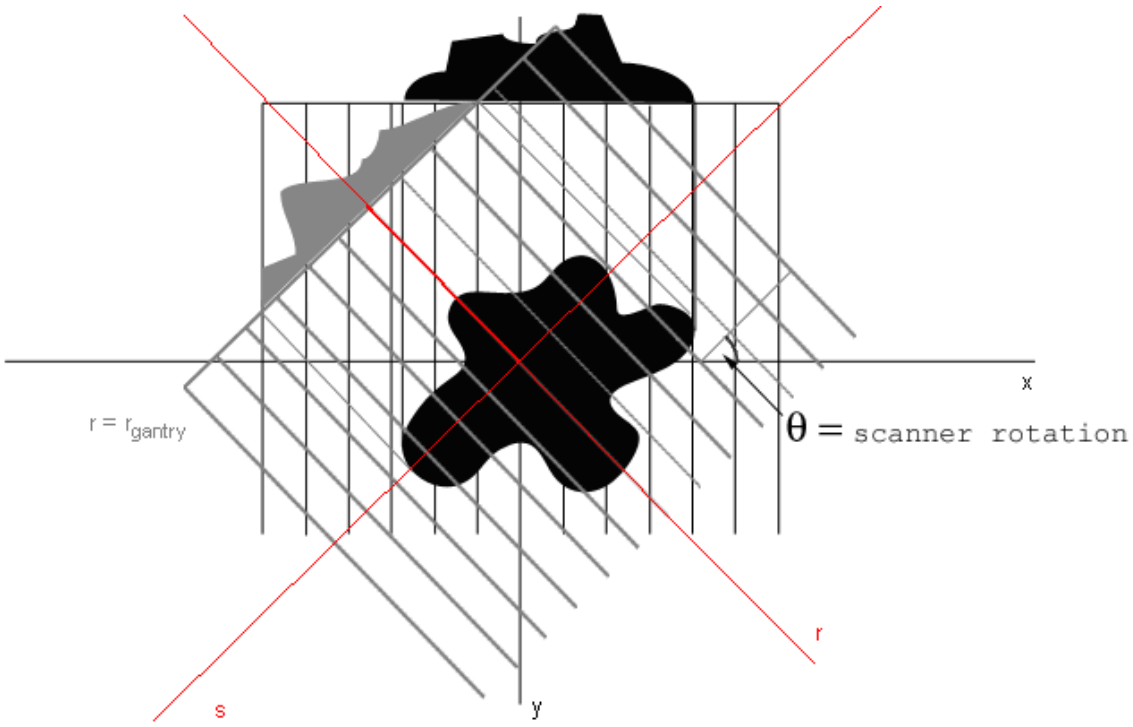

Figure 15. Ray projections along the 'r' axis with the detector array along the 's' axis at gantry radius.

Solving the r component of Eq. 3 for y and substituting the resulting factors into Equation Eq. 1 allows the direct calculation of the distance between a given ray and point via Eq. 4 where *rr* is the ray number (detector widths from detector home/beginning of the array) along the detector array.

$$d = \left\| x \cdot \cos\theta - y \cdot \sin\theta - rr \right\| \qquad (4)$$

Calculating the exact non-integer ray then rounding to the surrounding integer rays proved to be more computationally efficient. The distance between the ideal ray and the integer rays became the basis for the area calculation. If a ray boundary did not pass through the circle, the entire pixel approximation lay within a single ray region and the

reconstruction effectively defaults to a right hand justified neighbor approximation for pixel value as seen in Figure 16.

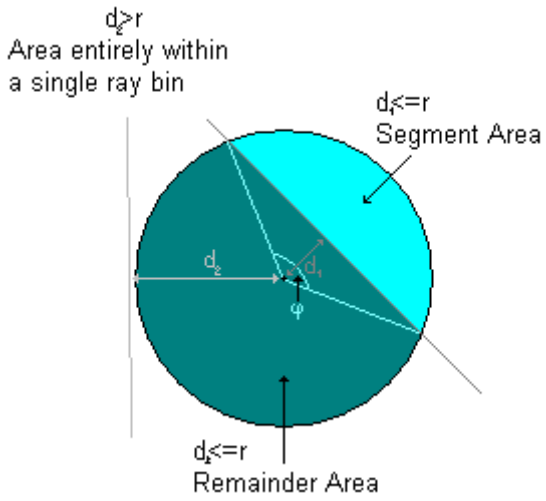

Figure 16.Ray circle approximation interaction showing the two possibilities of a ray boundary within and outside of the circle approximation and the resulting area values. For the internal ray boundary, the central angle φ is illustrated.

The other possibility illustrated in Figure 12 is a ray boundary that passes through the circle with the area now divided between two ray regions. Capitalizing on circular symmetry, any ray passing through the circle can be treated the same as any other of the same distance from the origin. The area of a segment of a circle is defined by Eq. 5, where φ is the central angle, d is the ray distance, and R is the radius of the circle.

$$A_s = \frac{R^2}{2} \cdot \left(\varphi - \sin\varphi\right) \tag{5}$$

Solving for φ using the right triangle formed by the radius and d, Eq. 5 becomes directly solvable in the form of Eq. 6.

$$A_s = R^2\left(\sin^{-1}\left(\frac{d}{R}\right) - \frac{\sin\left(2\cdot\cos^{-1}\left(\frac{d}{R}\right)\right)}{2}\right) \tag{6}$$

Because the parameters of the mapping only allow a maximum of two rays to contribute to a pixel, the remaining area is completely associated with the second ray. This limits the maximum radius of the circle to 1.0 pixels as well.

The majority of the computational work described above can be stored in a predefined maps corresponding to the scan parameters. Because these maps are pregenerated, accuracy becomes the driving factor in determining the circle value to use for a given reconstruction as processing time for the reconstruction is virtually identical between small and large circle diameters after the maps are created. Reconstruction accuracy measures mirror the importance of CT data to the medical and industrial communities; edge definition/migration and pixel value (radiodensity) shifts.

Map files are quite large, ranging from 800Kb to 151Mb for weight value maps at single floating point precision. Each map set contains four 3D matrixes of image sized arrays for each projection angle to track the segment and remainder areas as well as the associated ray values for each area segment. In total the reconstruction library takes approximately 20Gb of memory.

Image Reconstruction: Filtered linear backprojection was used to reconstruct images in this study. To correct for artifacts inherent in both synthetic and physical scanners, the bulk scan must be filtered before reconstruction. The "Shepp-Logan" filter (L. A. Shepp and B. F. Logan, 1974) was chosen for its reduced sensitivity to high frequency noise compared to a simple ramp filter like the "Ram-Lak" ***(Ramachandran & Lakshminarayanan, 1971)***. This filter consists of a low to high frequency ramp filter modified with a sinc function as defined in Eq. 7, and displayed graphically in Figure 7; where $H(f)$ is the filter mask, f_c is the Nyquist cut off frequency, and f is the spatial frequency ***(Jackson, 2005)***.

$$H(f) = \frac{2 \cdot f_c}{\pi} \cdot \sin\left(\pi \cdot \frac{\|f\| \cdot \pi}{2 \cdot f_c}\right) \quad \text{for } f<f_c \tag{7}$$

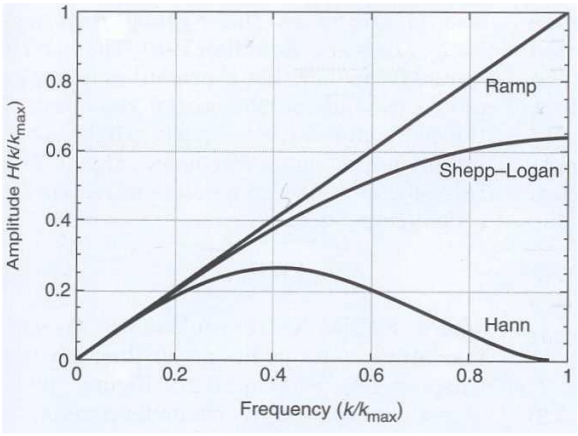

Figure 17. Graphs of Fourier Transform Filters **(Jackson, 2005)**

For consistency, the Nyquist is not optimized but locked at 1; however this compromise results in the ray like artifacts present Figure 18.

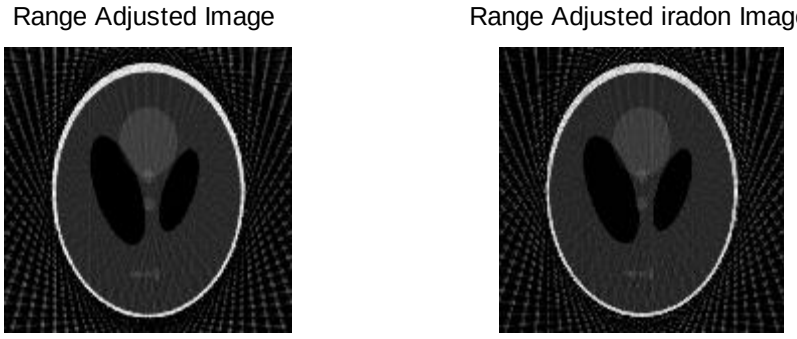

Figure 18. Reconstructions showing the ray like noise present in both the reconstruction and 'iradon' images with a Nyquist frequency of 1.

The scan is first expanded to the next power of two with respect to the square of the height of the scan to reduce aliasing and capitalize on MatLab's base two processing efficiency. This expanded scan is then run through MatLab's Fourier Transform function to convert the scan to frequency space. The filter *H (f)* is applied and the resulting scan inverse transformed back to the padded size in physical space. The scan is then cut back down to the correct size for reconstruction. For consistency, the entire filter process was copied from MatLab's built in 'iradon' inverse radon transform routine into the reconstruction algorithm to remove the filtering as a potential variable in comparing the reconstruction methods (Mathworks, Inc, 2004). The entire process can be seen as it is applied to a radon transform of a 256x256-5º "Shepp-Logan" image in Figure 15.

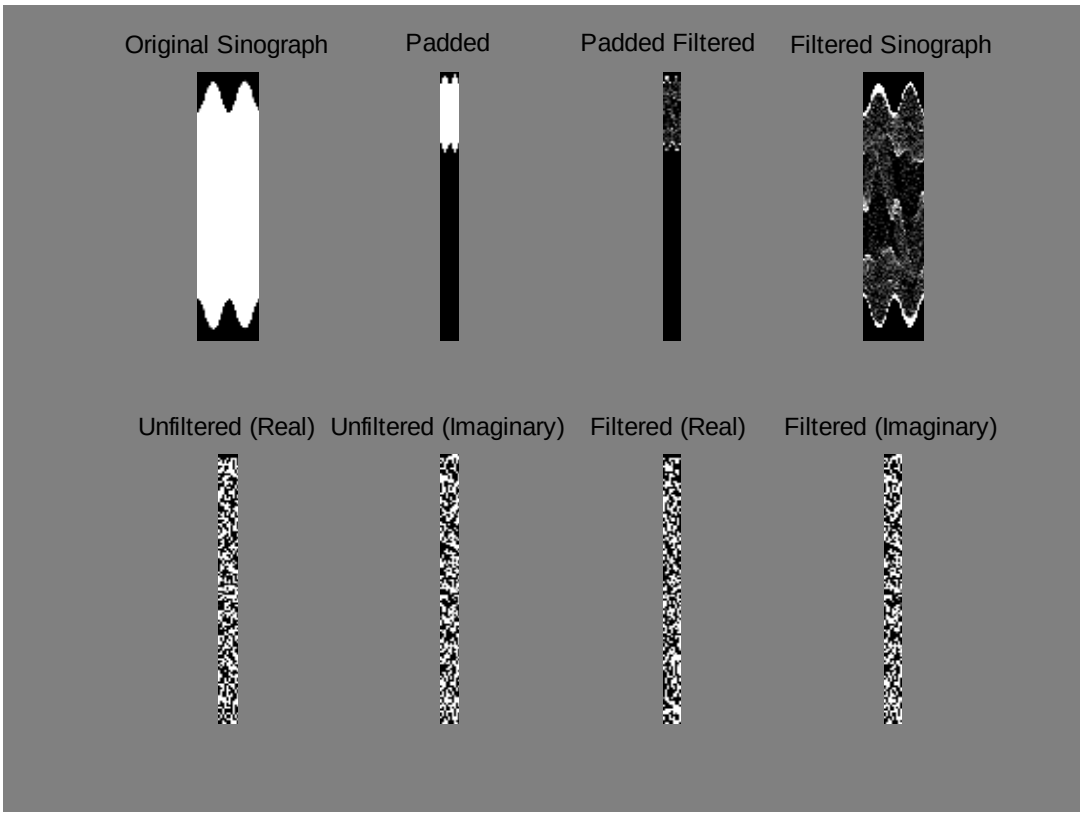

Figure 19. Original radon transform (signograph) through the full "Shepp-Logan" Fourier filtering process. Note: image range is from 0-1, the original radon transform is out of range.

The results of using an unfiltered scan are dramatically highlighted in Figure 16 where any usable detail is washed out of the image with just a rough shape visible.

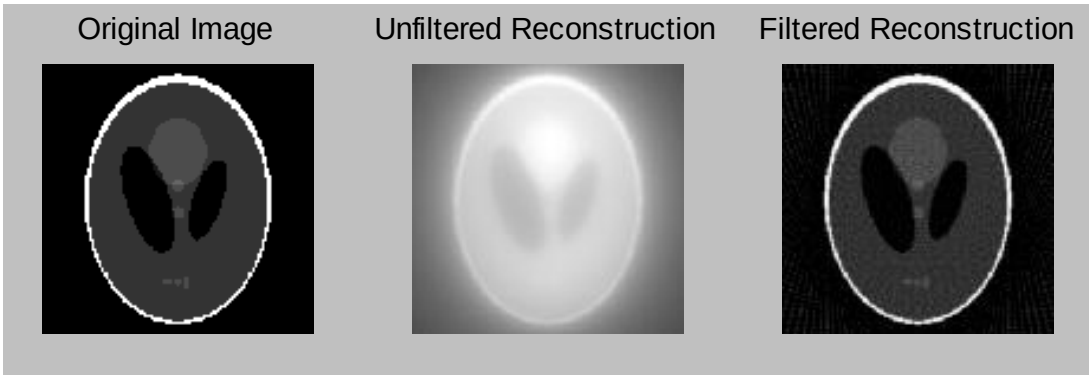

Figure 20. Unfiltered backprojection and "Ram-Lak" filtered backprojection as compared to the original 200x200 pixel "Shepp-Logan" image.

From this filtered scan, the reconstruction algorithm reassembles the data by selecting the proper ray from the scan as determined by the ray index map and multiplying the value by the area of the circle it covers as defined by the segment maps. These individual pixels form a single projection map that is summed with the building image. After reconstruction, the image is normalized by multiplying by π then dividing by two times the number of rotational steps and the percentage of the pixel the circle covered. By using the MatLab .mat binary file type, storage requirements for each image is minimized.

Data Analysis: The usefulness of CT in either the medical or industrial inspection realms is dependent on the ability of the reconstruction to correctly identify the boundaries of regions inside of the medium and correctly determine the density of each region. Original images were used as the analysis template for all "standard" sized image families.

All analysis routines created a standardized spreadsheet that contains the mean and standard deviation of the densities, edge shift, and edge slopes for all image sizes, rotations, and circle approximation radii. The final analysis method was the comparison of the base image against itself, which verified that the analysis methods were working properly and that the edge slope values in particular were calculating identically.

Automatic Region and Edge Identification

For the "Shepp-Logan", Ring, and Noise image families, the original densities are known to be multiples of 0.1 ranging from 0.1 to 1 which facilitates binning the images by density value. The image is filtered to "tag" each density region with an integer value assigning to a certain density layer of the image. Structures of a specific density, whether contiguous or separate, all represent the components of a density layer of the image and are all tagged with the same integer. Each layer is subjected to an 'imerode' command which removes the outer layer of pixels of a given structure as seen in Figure 21 to back away from edge effects due to the modulation transfer function digitization of an edge.

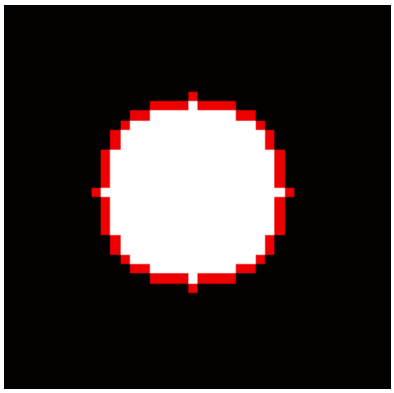

Figure 21. One pixel erosion of a 20 pixel radius circle highlighted in red.

The ‘imerode’ command also creates the know edges of the regions. To deconflict eroding a region into another, a possibility in an image such as the “Shepp-Logan” where there is a large constant density field, the eroded edge is used as a negative mask to remove any growth. The eroded image forms the density layer masks for use in finding the mean and standard deviation of the region. The eroded area is considered the edge with a positive mask as seen in Figure 22.

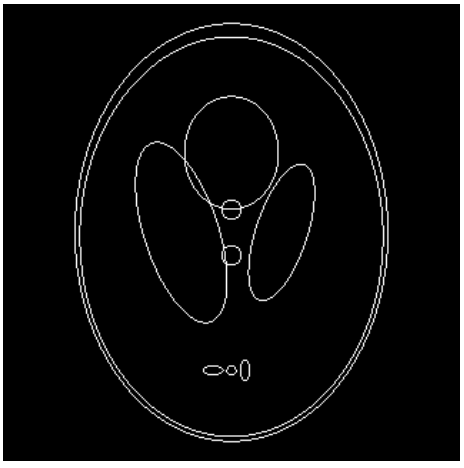

Figure 22. Positive edge mask of a 320x320 pixel “Shepp-Logan” phantom created by eroding a single pixel away from each “tagged” region of the original image.

Density analysis

Density of a region is critical to CT inspection of industrial parts for identification of material defects such as insufficient densification or porosity on castings. Medically, CT is often used for bone densitometry and other clinical processes requiring accurate density determination (Buzug, 2008). Since all density values of all three phantoms correspond to 0.n values, the values of each pixel in the reconstruction can be compared to its known value. The mean and standard deviation of the population of each "tagged" density region of the reconstruction after the imerode operation is calculated and recorded.

Edge shift

One of the most useful diagnostic characteristics of a CT image is that it can locate abnormalities and/or check the conformation of an object or structure to specifications. Fundamental to the proper function of this feature is the ability to identify an edge, or more properly a change in material density. In radiation therapy applications, the edges of a tumor define the treatment volume to be irradiated. An incorrectly calculated treatment volume can lead to unnecessary exposure of healthy tissue or insufficient exposure of the tumor mass. Either situation produces unacceptable side effects. Industrially, complex parts can be checked for conformation to a design spec where internal passages must meet size tolerances. If an edge were to migrate in the reconstruction, parts could be rejected needlessly or more significantly; defective parts make it past quality control.

Automated reconstructed image edge identification

The edge mask is used as a trigger for searching a 3x3 pixel neighborhood of the reconstructed image centered on the edge trigger for the pixel with maximum difference from its eight neighbors. Since it is possible for multiple pixels in the analysis region to have the same difference from its neighbors as others, the center pixel is considered to be the edge if it contains a maximal difference value.

Simplified edge definition algorithm

While in this study, we have the foreknowledge of where the edge should lie, edges in a target medium are not always known. Edge detection algorithms are dependent on the difference between one region and its neighbors so good digitization of an edge must be produced by the reconstruction. To simplify the edge digitization metric, edge slope was used. Edge slope is the average change in density across a vectorized gradient defined by the digitized edge. Edge slope is calculated as the difference of the center point from the neighbors along the vector from the maximal difference to the minimal difference. Since the analysis region is 3x3, these regions are either a pair of adjacent edges and the center pixel or a single edge and the middle row or column as diagramed in Figure 23.

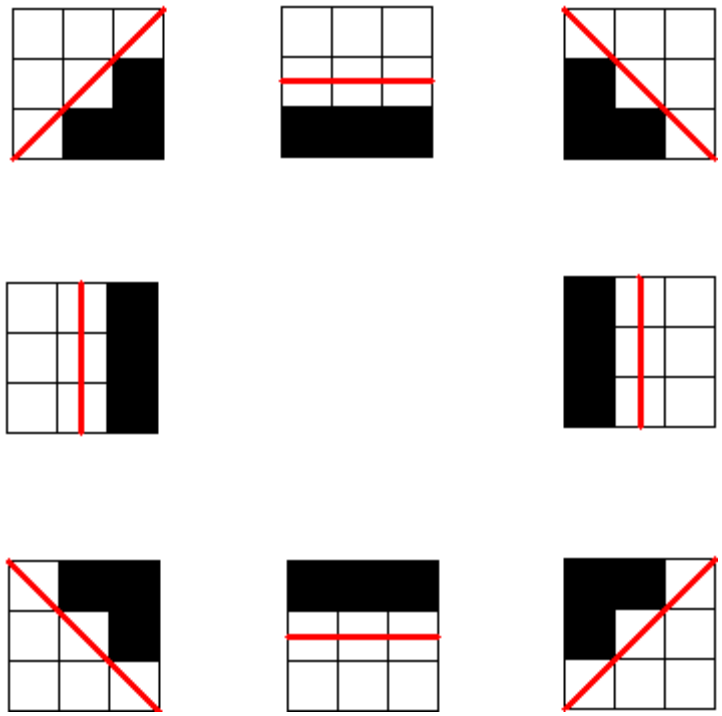

Figure 23. Possible edge slope masks depending on edge orientation determined by pixel difference gradient within the 3x3 neighborhood of the edge trigger. White squares signify a '1' in the mask while black squares signify a '0' in the mask. The red lines indicate the edge through the neighborhood.

Again these values are stored and the mean and standard deviation of the slopes calculated. An identical vectorized edge slope process is repeated for the base image to provide a benchmark to compare the reconstruction algorithms performance.

Analysis of oversized images

For oversized images, MatLab's 'iradon' function provides a known standard to compare the experimental reconstructions against. The 'iradon' function operates using the Inverse Radon Transform of the scan using the approximations of 2nd order ray distance weighting for pixel value assignment and a selectable filter (Mathworks, Inc, 2004). The

"Shepp-Logan" filter was used to match the experimental reconstruction filter type and the Nyquist limit was similarly locked at 1. The analysis process begins with the selection of the original scan to match the detector number and rotational step size of the experimental reconstruction to be analyzed. This scan is reconstructed using the 'iradon' function to create the known standard for oversized reconstruction comparison. By using the original image condition of binning into 0.n density bins, the 'iradon' reconstruction is binned based on the weighted average of the bin and its x±1 and y±1 neighbors rounded to the nearest 0.n bin. This weighted binning scheme provides a more spatially accurate binning of the values since pixel values near 0.n5 could be wrongly binned into a lower or higher bin based on straight rounding of the pixel value. For values out of the 0-1 range, the pixels are binned with the extremes. Beyond these special concessions to the lack of an initial image, the analysis process is otherwise identical to the "standard" sized image analysis method. The oversized image set consisted solely of a 1490x1490 pixel image compressed into a 512x512 pixel scan and reconstruction of each image for all rotational step sizes and circle radii.

Optimized circle radius

It is possible using the above listed performance measures to calculate the optimal circle size for a given image size and rotational combination for each image family. The optimization was done both for individual measures and the overall reconstruction. All image measures are weighted evenly in the overall optimization, though customized weights for a given parameter could be applied in the optimization routine. The individual optimum for a measured parameter is a calculation of the absolute difference

between the reconstructed parameter value and the original "true" value from the base image. Since density accuracy is measured in 10 regions, the total difference between of all density regions and their corresponding true value is used. Edge shift and edge slope both use the straight numeric difference of the parameters from the optimal value (0) for shift, and the phantom edge slope for edge slope. The circle radius with the smallest difference is the optimal value. The differences of all measures for a given radius are summed and the radius with the smallest total absolute difference is the overall optima for that phantom, image size, and rotational step size.

RESULTS

The three image families, “Shepp-Logan”, Ring, and Noise; were scanned, reconstructed, and analyzed in terms of edge position, edge slope (definition), and density. The images were first reconstructed using the custom built algorithm.

Standard sized reconstructions: The standard sized images, 128x128 - 512x512 pixels, reconstructions were analyzed using the original phantom image as the standard of comparison.

Qualitative effect of circle radius

Figures 24-26 illustrate the progressively improving reconstruction quality as the circle approximation size grows.

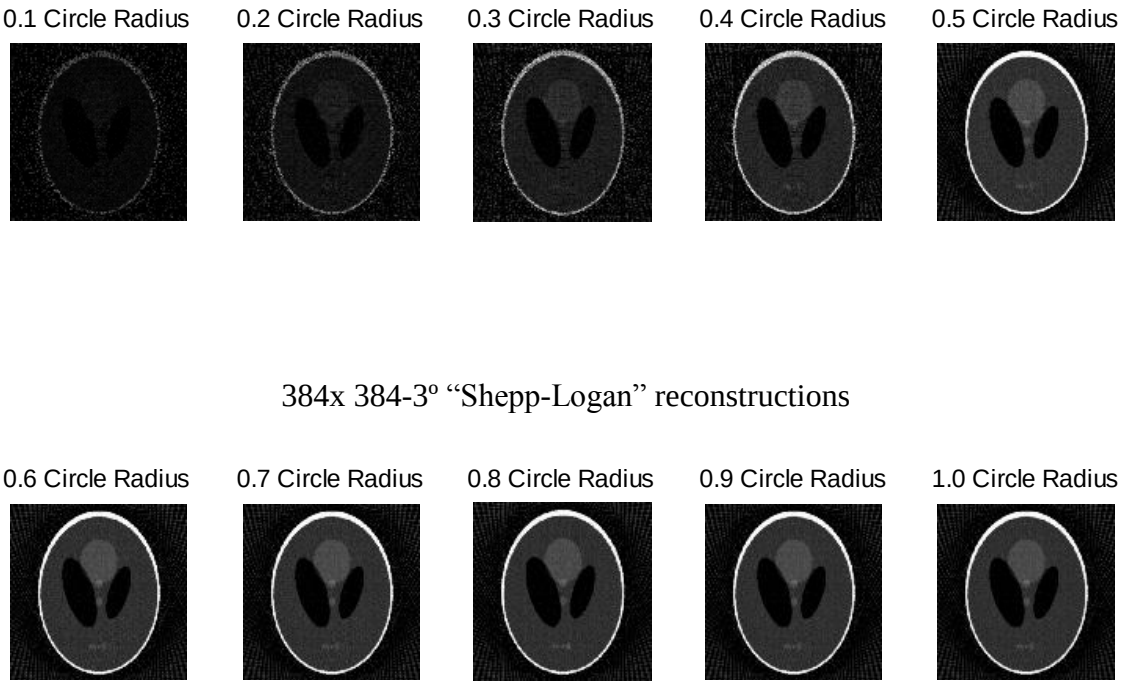

Figure 24. Reconstructions of the 384x384-3º "Shepp-Logan" Phantom using circle radii of 0.1-1.0 pixels.

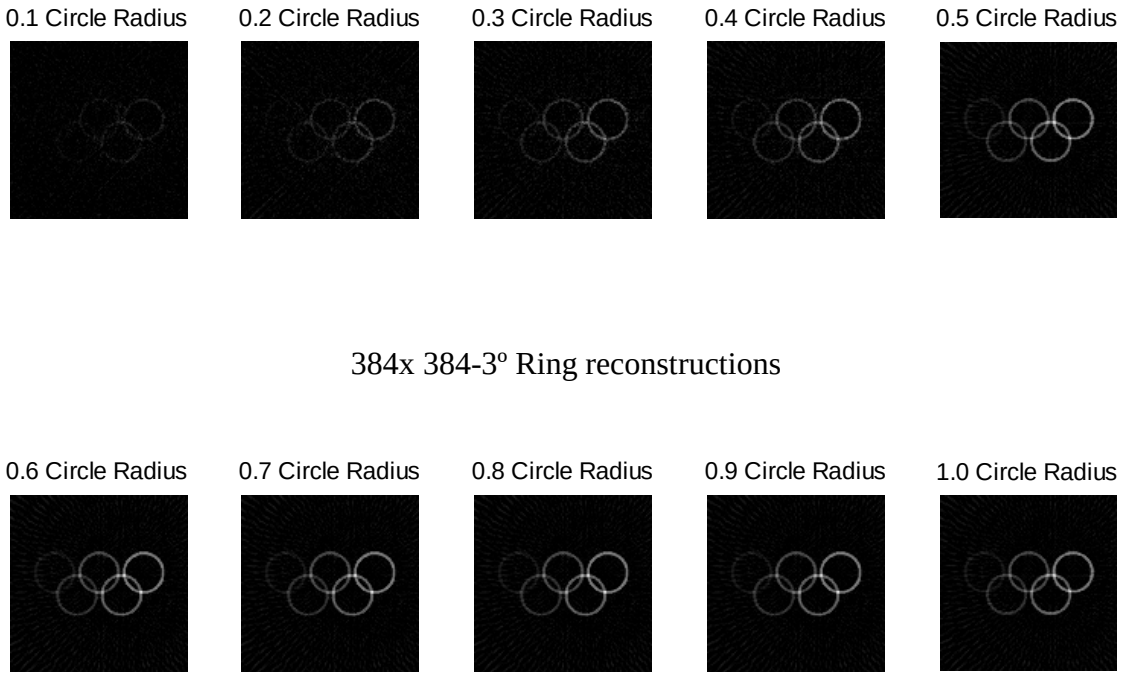

Figure 25. Reconstructions of the 384x384-3º Ring Phantom using circle radii of 0.1-1.0 pixels.

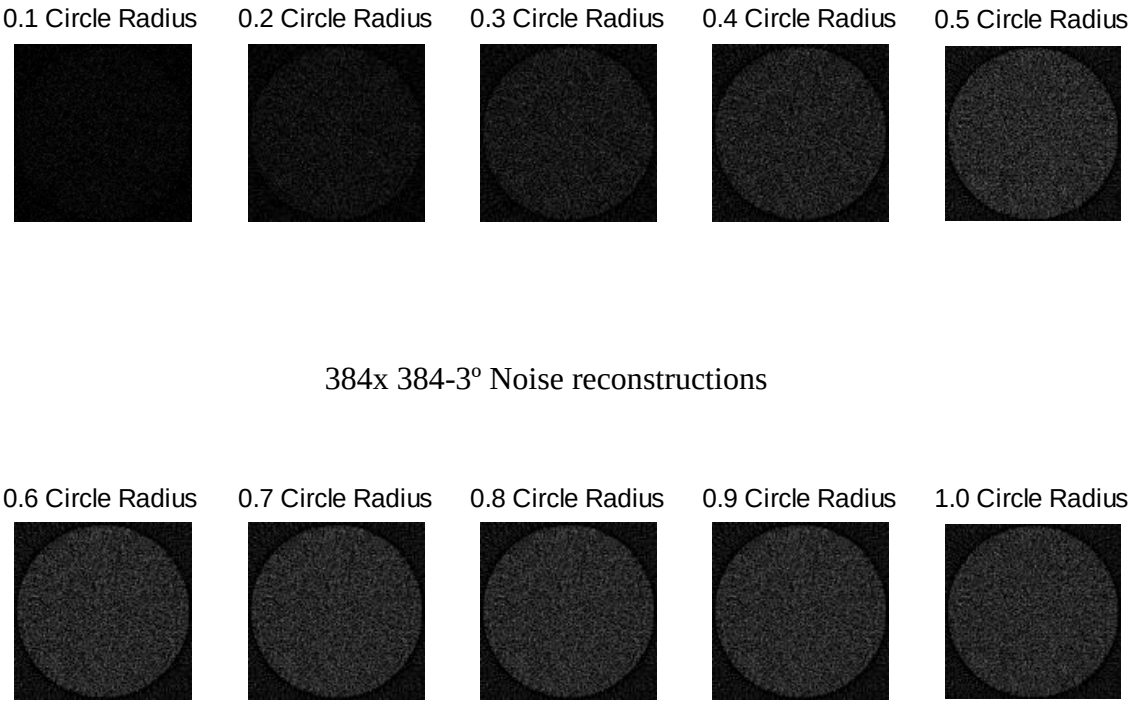

Figure 26. Reconstructions of the 384x384-3º Noise Phantom using circle radii of 0.1-1.0 pixels.

Images reconstructed with less than a 0.5 pixel radius are of poor quality and structures are very poorly defined. After the radii reaches 0.5, the quality of the image largely stabilized and only minor difference are observed. Because of its greater content, the Noise phantom exhibits many more artifacts in the "unscanned" region outside of the full width inscribed circle but does show a definitive ring that is the boundary of the real data.

Density accuracy

Each image was likewise evaluated for density accuracy for all image sizes, rotational step sizes, and circle radii. The reconstruction intensity was compared to the intensity of the original image for the 0.3 density regions for all circle radii as well as the identical region in the "iradon" reconstruction. The 0.3 density region was chosen for its presence

in all three phantoms and it's large abundance in the "Shepp-Logan" and Ring phantoms. The results for the "Shepp-Logan" phantom are shown in Table 1 for selected image sizes.

Table 1. Intensity values in the 0.3 region of the reconstructed image for all circle radii and the 'iradon' reconstruction of the "Shepp-Logan" phantom.

Density = 0.3	256x256		384x384		512x512	
Reconstruction type	Mean	Standard Deviation	Mean	Standard Deviation	Mean	Standard Deviation
iradon	0.294	0.021	0.297	0.022	0.295	0.022
0.1	0.129	0.042	0.110	0.038	0.099	0.034
0.2	0.169	0.036	0.150	0.033	0.140	0.031
0.3	0.223	0.035	0.206	0.034	0.192	0.032
0.4	0.241	0.029	0.241	0.030	0.231	0.029
0.5	0.286	0.022	0.286	0.022	0.267	0.021
0.6	0.288	0.021	0.288	0.021	0.269	0.020
0.7	0.289	0.020	0.289	0.020	0.271	0.019
0.8	0.290	0.019	0.291	0.020	0.273	0.018
0.9	0.290	0.018	0.291	0.019	0.274	0.018
1.0	0.291	0.018	0.292	0.019	0.275	0.018

The results for the Ring phantom are shown in Table 2 for selected image sizes.

Table 2. Intensity values in the 0.3 region of the reconstructed image for all circle radii and the 'iradon' reconstruction of the Ring phantom.

Density = 0.3	256x256		384x384		512x512	
Reconstruction type	Mean	Standard Deviation	Mean	Standard Deviation	Mean	Standard Deviation
iradon	0.263	0.070	0.282	0.062	0.288	0.056
0.1	0.214	0.137	0.187	0.134	0.165	0.116
0.2	0.220	0.094	0.226	0.107	0.232	0.105
0.3	0.253	0.093	0.253	0.091	0.244	0.086
0.4	0.287	0.090	0.266	0.075	0.269	0.072
0.5	0.285	0.078	0.296	0.066	0.294	0.058
0.6	0.285	0.077	0.296	0.065	0.294	0.058
0.7	0.285	0.077	0.296	0.065	0.295	0.057
0.8	0.285	0.076	0.296	0.065	0.295	0.057
0.9	0.285	0.076	0.296	0.064	0.295	0.057
1.0	0.285	0.075	0.296	0.064	0.295	0.057

The results for the Noise phantom are shown in Table 3 for selected image sizes.

Table 3. Intensity values in the 0.3 region of the reconstructed image for all circle radii and the 'iradon' reconstruction of the Noise phantom.

Density = 0.3	256x256		384x384		512x512	
Reconstruction type	Mean	Standard Deviation	Mean	Standard Deviation	Mean	Standard Deviation
iradon	0.242	0.048	0.248	0.055	0.246	0.062
0.1	0.146	0.074	0.133	0.074	0.101	0.065
0.2	0.198	0.068	0.181	0.070	0.156	0.071
0.3	0.208	0.058	0.177	0.054	0.179	0.064
0.4	0.245	0.058	0.213	0.056	0.205	0.063
0.5	0.254	0.053	0.235	0.054	0.217	0.058
0.6	0.254	0.052	0.236	0.053	0.219	0.057
0.7	0.254	0.051	0.237	0.052	0.220	0.056
0.8	0.255	0.050	0.237	0.051	0.221	0.056
0.9	0.256	0.049	0.238	0.050	0.222	0.055
1.0	0.256	0.049	0.238	0.050	0.223	0.055

Overall the density accuracy improves as the circle radius becomes larger. The density accuracy is terrible below 0.4 pixels radius for all cases. Density accuracy for the 0.3 region improves at 0.5 pixels radius and gets incrementally better, though in very small steps, as the radius increases. Interestingly, larger images of the "Shepp-Logan" and Noise phantoms have 3% and 7% worse density accuracy at 512x512 pixels than they do at 256x256 pixels respectively.

Edge shift

From the perspective of radiation therapy the most critical parameter of any CT reconstruction is the edge precision, that is the ability of the reconstruction to identify the edge of an internal structure for treatment. All images were tested against the original for edge shift and both the reconstruction and the 'iradon' exhibited zero edge shift.

Edge slope

Tables 4-6 shows the edge slope values as compared to the original phantom image and 'iradon' for selected image sizes of each of the image families.

Table 4. Edge Slope values for the original "Shepp-Logan" phantom image and selected reconstructed image sizes for the 2º rotational step size for the 'iradon' and reconstruction.

"Shepp-Logan"	256x256		384x384		512x512	
Reconstruction Type	Mean	Standard Deviation	Mean	Standard Deviation	Mean	Standard Deviation
phantom	**0.543**	**0.317**	**0.541**	**0.316**	**0.541**	**0.316**
iradon	0.563	0.35	0.641	0.409	0.639	0.41
0.1	0.115	0.087	0.123	0.095	0.122	0.096
0.2	0.232	0.162	0.243	0.171	0.24	0.174
0.3	0.351	0.234	0.367	0.249	0.359	0.248
0.4	0.471	0.307	0.488	0.322	0.48	0.323
0.5	0.602	0.39	0.63	0.408	0.621	0.408
0.6	0.601	0.387	0.629	0.406	0.62	0.406
0.7	0.6	0.385	0.627	0.404	0.618	0.404
0.8	0.598	0.383	0.625	0.402	0.616	0.403
0.9	0.597	0.38	0.625	0.401	0.615	0.402
1	0.596	0.379	0.623	0.4	0.614	0.401

Table 5. Edge Slope values for the original Ring phantom image and selected reconstructed image sizes for the 2º rotational step size for the 'iradon' and reconstruction.

Ring	256x256		384x384		512x512	
Reconstruction Type	Mean	Standard Deviation	Mean	Standard Deviation	Mean	Standard Deviation
phantom	**0.227**	**0.161**	**0.23**	**0.169**	**0.23**	**0.168**
iradon	0.275	0.193	0.281	0.202	0.281	0.203
0.1	0.052	0.041	0.054	0.044	0.054	0.045
0.2	0.104	0.079	0.105	0.083	0.106	0.083
0.3	0.154	0.113	0.158	0.119	0.159	0.121
0.4	0.208	0.15	0.212	0.156	0.211	0.158
0.5	0.27	0.189	0.277	0.2	0.276	0.201
0.6	0.269	0.188	0.277	0.199	0.276	0.2
0.7	0.269	0.187	0.276	0.198	0.275	0.2
0.8	0.268	0.186	0.276	0.197	0.274	0.198
0.9	0.267	0.186	0.275	0.197	0.273	0.198
1	0.267	0.185	0.275	0.197	0.273	0.197

Table 6. Edge Slope values for the original Noise phantom image and selected reconstructed image sizes for the 2º rotational step size for the 'iradon' and reconstruction.

Noise	256x256		384x384		512x512	
Reconstruction Type	Mean	Standard Deviation	Mean	Standard Deviation	Mean	Standard Deviation
phantom	**0.207**	**0.058**	**0.21**	**0.059**	**0.21**	**0.057**
iradon	0.219	0.055	0.225	0.06	0.222	0.064
0.1	0.039	0.018	0.042	0.021	0.04	0.023
0.2	0.078	0.028	0.084	0.032	0.079	0.035
0.3	0.118	0.037	0.126	0.042	0.119	0.046
0.4	0.157	0.045	0.168	0.051	0.159	0.054
0.5	0.202	0.054	0.215	0.059	0.205	0.063
0.6	0.201	0.054	0.215	0.059	0.205	0.063
0.7	0.201	0.053	0.215	0.058	0.205	0.062
0.8	0.201	0.053	0.215	0.057	0.205	0.061
0.9	0.201	0.052	0.215	0.057	0.205	0.061
1	0.201	0.052	0.215	0.057	0.205	0.061

Interestingly, the edge slope follows an inverse pattern from the density accuracy with decreasing slope values as the circle size becomes larger. This is indicative of greater contrast difference between the two regions contained in the 3x3 edge neighborhood and would show greater edge definition. Additionally, image size did not have a significant impact on the accuracy of the edge slope. There is no clear pattern to the circle radius that the image has minimal variation from the phantom that appears tied to image size.

Optimum Circle Radius: The optima for the Shepp and Logan are shown in Tables 7 and graphically in Figure 27.

Table 7.Optimal circle radii for the "Shepp-Logan" Phantom

5º steps	128	192	256	320	384	448	512
Edge Shift	0	0	0	0	0	0	0
Edge Slope	0.6	1	1	1	1	1	1
Density	0.5	0.5	0.5	0.5	0.5	0.5	0.5
Overall	**0.5**	**1**	**1**	**1**	**1**	**1**	**1**
4º steps	128	192	256	320	384	448	512
Edge Shift	0	0	0	0	0	0	0
Edge Slope	0.5	1	1	1	1	1	1
Density	0.5	0.5	0.5	0.5	0.5	0.5	0.5
Overall	**0.5**	**1**	**1**	**1**	**1**	**1**	**1**
3º steps	128	192	256	320	384	448	512
Edge Shift	0	0	0	0	0	0	0
Edge Slope	0.5	1	1	1	1	1	1
Density	0.5	0.5	0.5	0.5	0.5	0.5	0.5
Overall	**0.5**	**1**	**1**	**1**	**1**	**1**	**1**
2º steps	128	192	256	320	384	448	512
Edge Shift	0	0	0	0	0	0	0
Edge Slope	0.5	1	1	1	1	1	1
Density	0.5	0.5	0.5	0.5	0.5	0.5	0.5
Overall	**0.5**	**1**	**1**	**1**	**1**	**1**	**1**

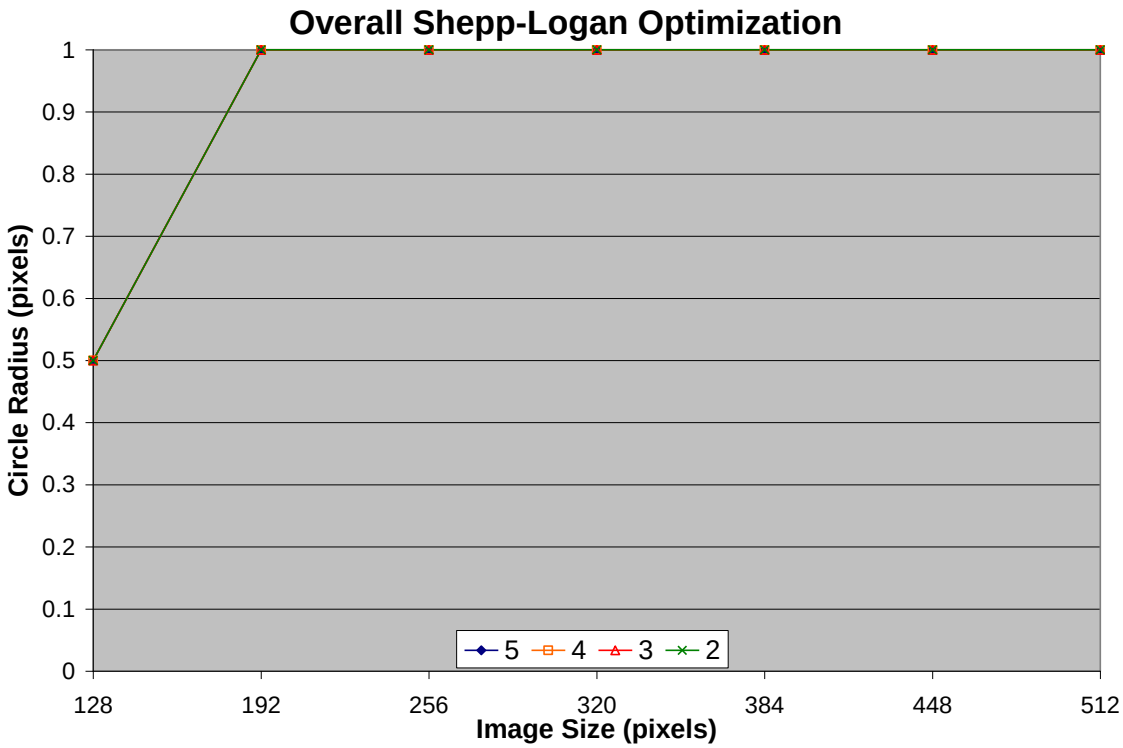

Figure 27. Overall circle radius optimization for the “Shepp-Logan” Phantom.

Similarly the individual and overall optima for the Ring Phantom are plotted in Tables 8 and Figure 28.

Table 8. Optimal circle radii for the Ring Phantom with

5º steps	128	192	256	320	384	448	512
Edge Shift	0	0	0	0	0	0	0
Edge Slope	0.5	1	0.4	0.4	0.4	0.4	0.4
Density	1	0.5	0.5	0.5	0.5	0.5	0.5
Overall	**0.5**	**0.5**	**0.5**	**0.5**	**0.5**	**0.6**	**1**
4º steps	128	192	256	320	384	448	512
Edge Shift	0	0	0	0	0	0	0
Edge Slope	0.5	1	0.4	0.4	0.4	0.4	0.4
Density	0.5	0.5	0.5	0.5	0.5	0.5	0.5
Overall	**0.5**	**0.5**	**0.5**	**0.5**	**0.5**	**0.5**	**0.5**
3º steps	128	192	256	320	384	448	512
Edge Shift	0	0	0	0	0	0	0
Edge Slope	0.5	1	0.4	0.4	0.4	0.4	0.4
Density	0.5	0.5	0.5	0.5	0.5	0.5	0.5
Overall	**0.5**	**0.5**	**0.5**	**0.5**	**0.5**	**0.5**	**0.8**
2º steps	128	192	256	320	384	448	512
Edge Shift	0	0	0	0	0	0	0
Edge Slope	0.5	1	0.4	0.4	0.4	0.4	0.4
Density	1	0.5	0.5	0.5	0.5	0.5	0.5
Overall	**0.5**	**0.5**	**0.5**	**0.5**	**0.5**	**0.5**	**0.5**

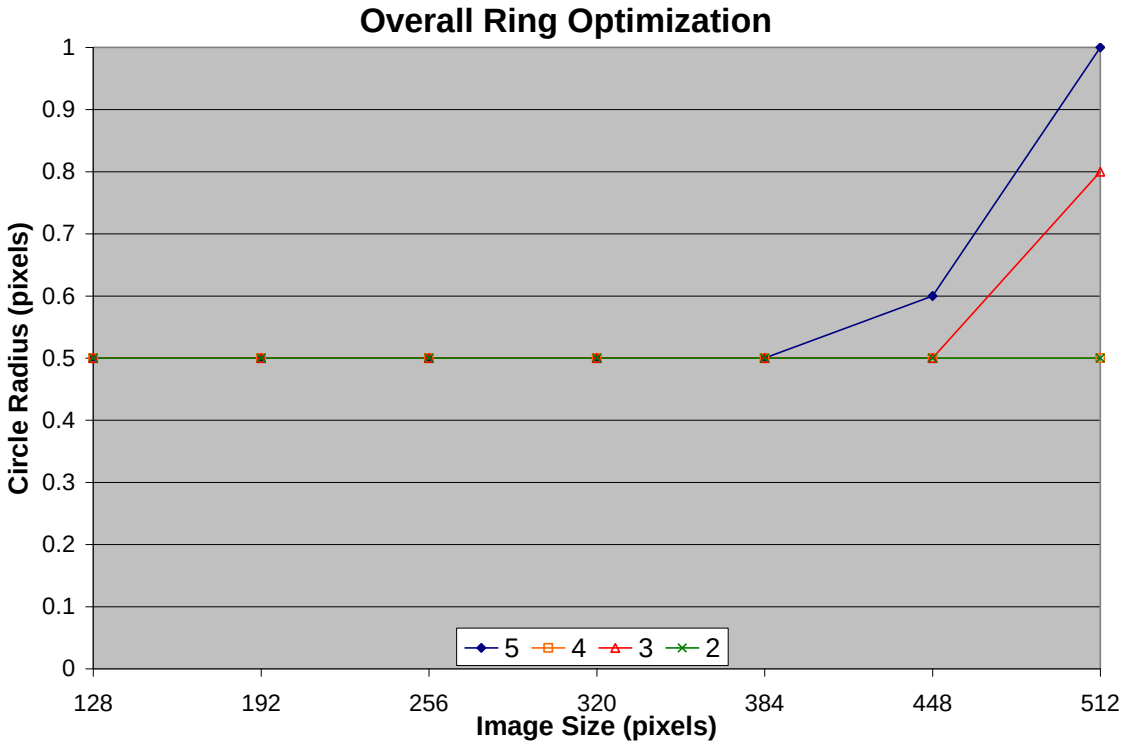

Figure 28. Overall circle radius optimization for the Ring Phantom.

Finally the individual and overall optima for the Noise Phantom are plotted in Tables 9 and Figure 29.

Table 9. Optimal circle radii for the Noise Phantom with

5º steps	128	192	256	320	384	448	512
Edge Shift	0	0	0	0	0	0	0
Edge Slope	0.5	1	0.5	1	1	0.6	0.5
Density	0.5	0.5	0.5	0.5	0.5	0.5	0.5
Overall	**0.5**	**0.5**	**0.5**	**0.5**	**0.5**	**0.5**	**0.5**
4º steps	128	192	256	320	384	448	512
Edge Shift	0	0	0	0	0	0	0
Edge Slope	0.5	1	0.5	1	1	0.8	0.5
Density	0.5	0.5	0.5	0.5	0.5	0.5	0.5
Overall	**0.5**	**0.5**	**0.5**	**0.5**	**0.5**	**0.5**	**0.5**
3º steps	128	192	256	320	384	448	512
Edge Shift	0	0	0	0	0	0	0
Edge Slope	0.5	1	0.5	1	1	0.9	0.5
Density	0.5	0.5	0.5	0.5	0.5	0.5	0.5
Overall	**0.5**	**0.5**	**0.5**	**0.5**	**0.5**	**0.5**	**0.5**
2º steps	128	192	256	320	384	448	512
Edge Shift	0	0	0	0	0	0	0
Edge Slope	0.5	1	0.5	1	1	0.5	0.5
Density	0.5	0.5	0.5	0.5	0.5	0.5	0.5
Overall	**0.5**	**0.5**	**0.5**	**0.5**	**0.5**	**0.5**	**0.5**

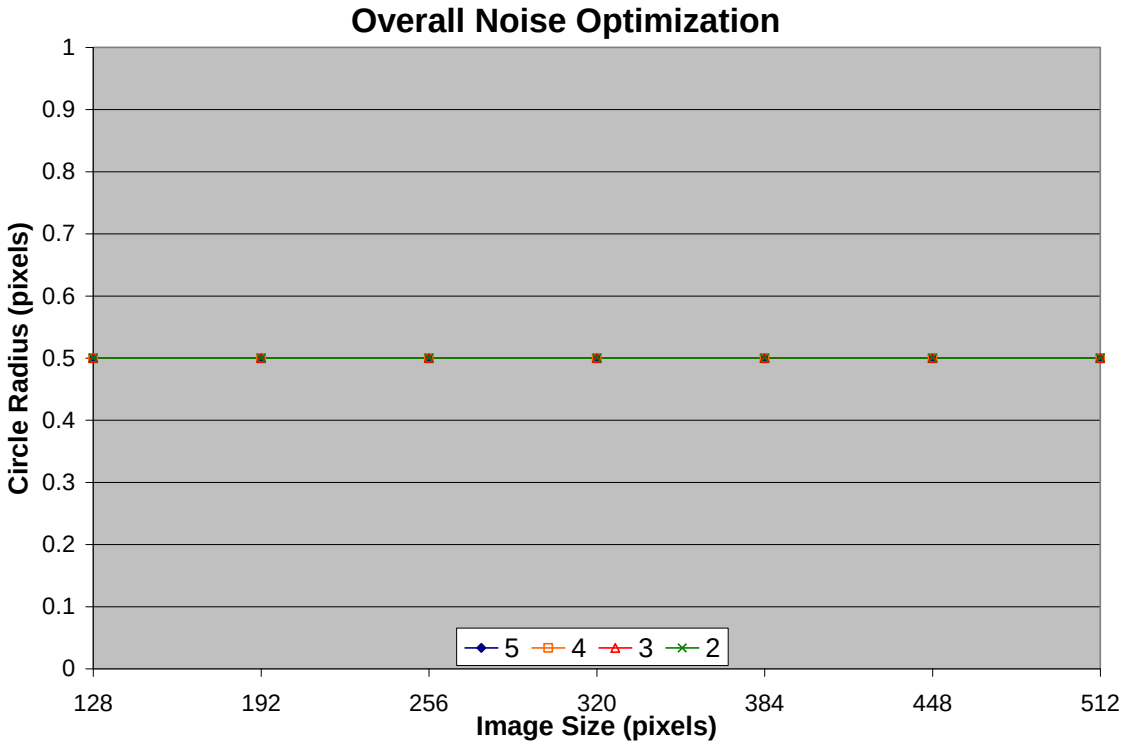

Figure 29. Overall circle radius optimization for the Noise Phantom

It is of interesting note that the minimal circle radius for all image families at is 0.5 pixels and is almost bimodal with optima occurring at the minimum stability point of 0.5 pixels or at maximum radius. There are a few outliers but only most are within 0.1 pixels radius off of one of these two modes. Similarly the individual optima cluster at 1.0 or 0.4 pixels for density and 0.4-0.6 or 1.0 pixels for edge slope. Larger images tend to generate higher circle radii optima as demonstrated by the shift from 0.5 pixel for the 128x128 pixel image to 1.0 pixel for the 192x192 pixel image and the 448x448 and 512x512 pixel optima for the Ring phantom.

Oversized images: The oversized versions of all three images were reconstructed using the same range of rotational steps and circle radii as with the "standard" sized images.

The following 3 figures show the progression of reconstructed images for all three image families at the 3º rotational step size

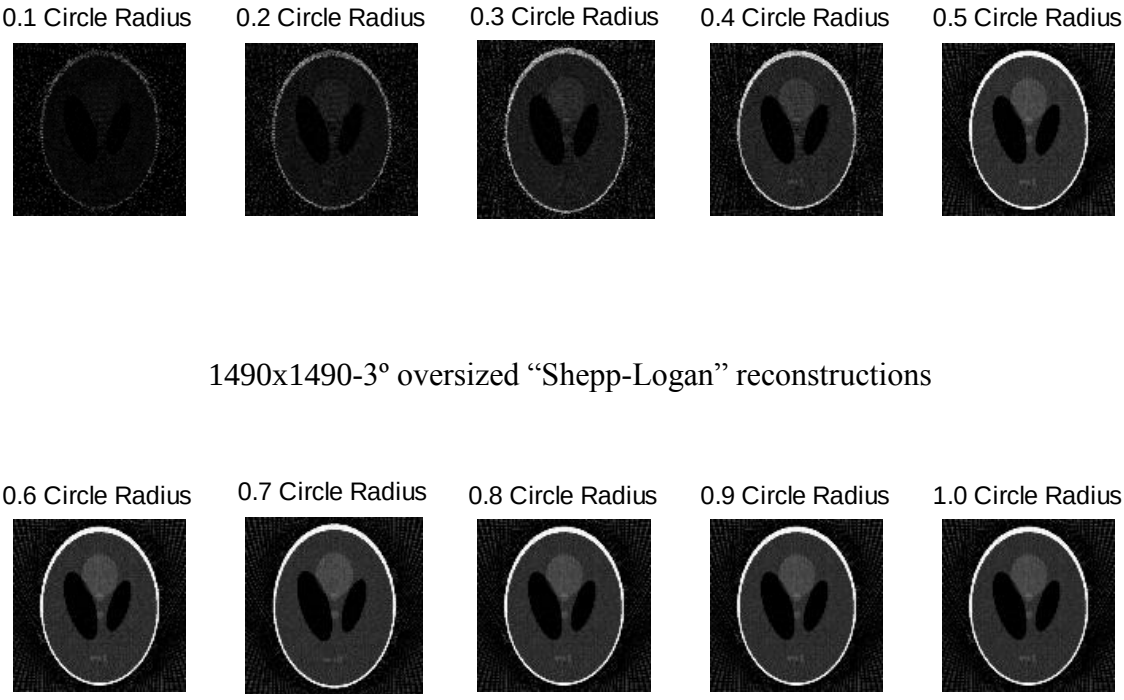

1490x1490-3º oversized "Shepp-Logan" reconstructions

Figure 30. Reconstructions of the 1490x1490 pixel "Shepp-Logan" phantom original image scanned and compressed to a 512x512-3º then reconstructed using circle radii of 0.1-1.0 pixels.

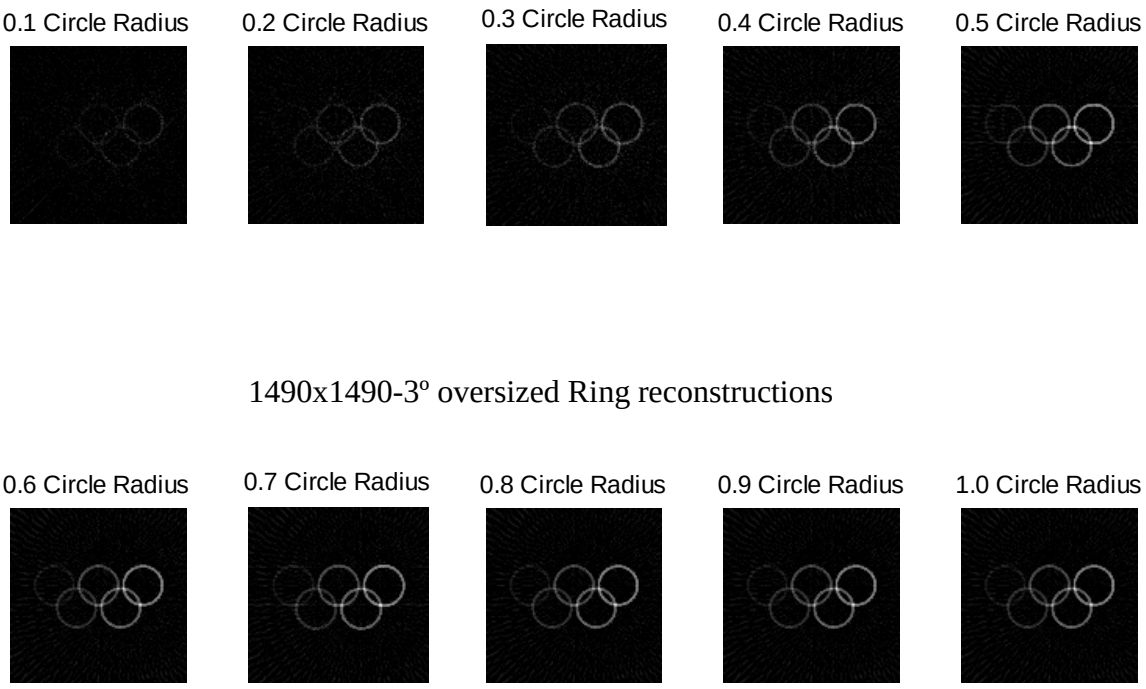

Figure 31. Reconstructions of the 1490x1490 pixel Ring phantom original image scanned and compressed to a 512x512-3º then reconstructed using circle radii of 0.1-1.0 pixels.

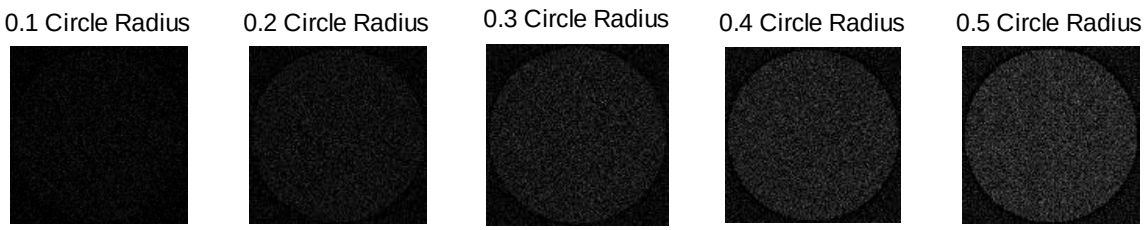

1490x1490-3º oversized Noise reconstructions

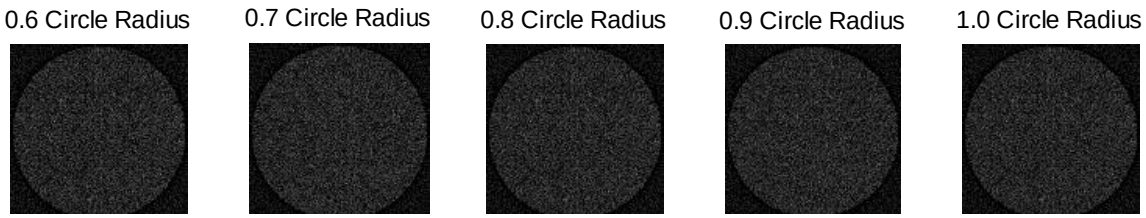

Figure 32. Reconstructions of the 1490x1490 pixel Noise phantom original image scanned and compressed to a 512x512-3º then reconstructed using circle radii of 0.1-1.0 pixels.

As with the "standard" sized images, the oversized images show increasing image quality as the circle radius increases. Again the image quality stabilizes at approximately 0.5 pixel circle radius. However the overall image quality is marginally better with the oversized images. Most noticeable is the increased signal to noise ratio in the Noise phantom with less noise in the "unscanned" areas.

The oversized images were also processed through the optimization algorithm though the region definition and edge slope values were determined off of the 'iradon' vs. the original images. The composite Table 10 shows the optimizations for each of the image

types for density, edge shift, and edge slope for all circle radii. Likewise Figure 33 shows the overall optimization graphically for equally weighted parameters.

Table 10. Circle radius optima for all density, edge shift, and edge slope for all three oversized images

5º	"Shepp-Logan"	Ring	Noise
Edge Shift	0	0	0
Edge Slope	0.5	0.5	0.5
Density	1	1	1
Overall	**0.5**	**1**	**1**
4º	"Shepp-Logan"	Ring	Noise
Edge Shift	0	0	0
Edge Slope	0.5	0.5	0.5
Density	0.6	1	1
Overall	**0.5**	**0.5**	**1**
3º	"Shepp-Logan"	Ring	Noise
Edge Shift	0	0	0
Edge Slope	0.5	0.5	0.5
Density	0.5	1	0.5
Overall	**0.5**	**0.5**	**0.5**
2º	"Shepp-Logan"	Ring	Noise
Edge Shift	0	0	0
Edge Slope	0.5	0.5	0.5
Density	1	1	0.5
Overall	**0.5**	**1**	**0.5**

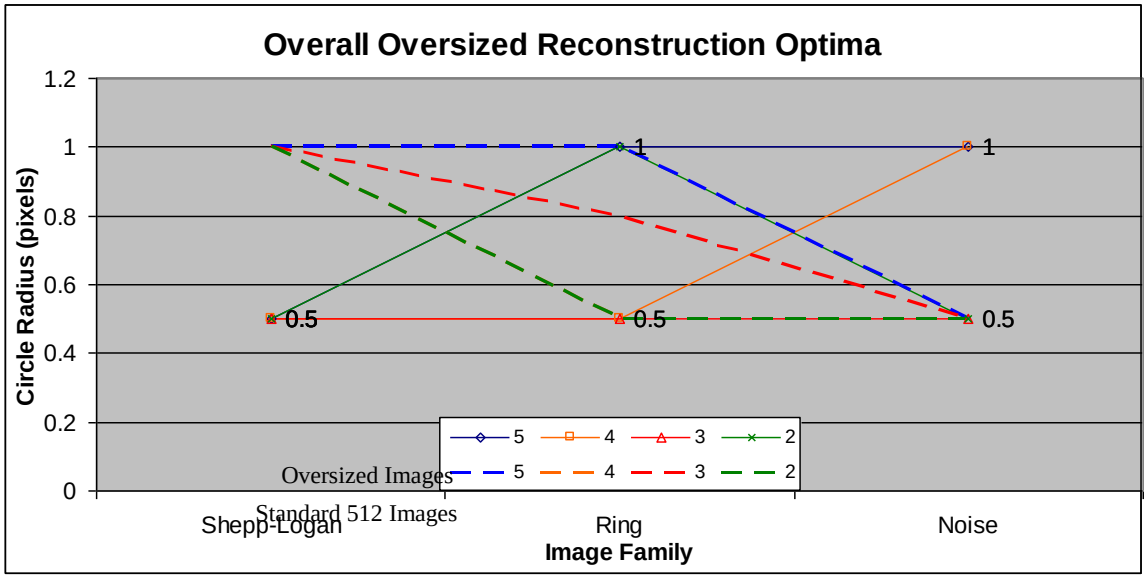

Figure 33. Overall circle radius optimization for oversized reconstructions of all three images against the optima of a 512x512 pixel image of the same family but "standard sized".

The optimization is once again bimodal with optima occurring at either the minimum value of 0.5 pixels for image stability or 1.0 pixels radius for maximum area coverage. While there is overlap between the optima for oversized and the comparable 512x512 pixel reconstruction, the cases of non-overlap are quite dramatic with the optima reverting to the modal opposite of the 512x512 "standard" optima.

DISCUSSION

Based upon the qualitative analysis of the images themselves and the numerical analysis of the image measures, the alternative reconstruction does not produce an image of noticeably better quality than the conventional linear interpolation method. On a 95% confidence interval, the alternative reconstruction is statically similar to the 'iradon' representation of the linear approximation technique for radius values over 0.4 pixels for all but two cases in the Noise phantom with an image size of 192x192 pixels and rotational step sizes of 2 and 3º. See Table 11 for the stoplight chart. Green is 100% failure to reject the null hypothesis of similar populations, yellow is a conditional failure to reject the null hypothesis with the range of failure marked in the cell and red is 100% rejection of the null hypothesis.

Table 11. Stoplight chart of the 95% confidence interval Z-test comparison of the alternative reconstruction against the ‘iradon’ reconstruction for 5-2° rotational step sizes.

“Shepp-Logan” 95% Confidence Interval Z-test

Density	5°	4°	3°	2°	Edge Slope	5°	4°	3°	2°
128	>=0.5	>=0.5	>=0.5	>=0.5	128	>=0.3	>=0.3	>=0.3	>=0.3
192	>=0.5	>=0.5	>=0.5	>=0.5	192	>=0.3	>=0.3	>=0.3	>=0.3
256	>=0.5	>=0.5	>=0.5	>=0.5	256	>=0.4	>=0.4	>=0.4	>=0.4
320	>=0.5	>=0.5	>=0.5	>=0.5	320	>=0.4	>=0.4	>=0.4	>=0.4
384	>=0.5	>=0.5	>=0.5	>=0.5	384	>=0.4	>=0.4	>=0.4	>=0.4
448	>=0.5	>=0.5	>=0.5	>=0.5	448	>=0.4	>=0.4	>=0.4	>=0.4
512	>=0.5	>=0.5	>=0.5	>=0.5	512	>=0.4	>=0.4	>=0.4	>=0.4

Ring 95% Confidence Interval Z-test

Density	5°	4°	3°	2°	Edge Slope	5°	4°	3°	2°
128					128				
192	>=0.5	>=0.5			192				
256	>=0.5	>=0.5	>=0.5	>=0.5	256				
320	>=0.5	>=0.5	>=0.5	>=0.5	320				
384	>=0.5	>=0.5	>=0.5	>=0.5	384				
448	>=0.5	>=0.5	>=0.5	>=0.5	448				
512	>=0.5	>=0.5	>=0.5	>=0.5	512				

Noise 95% Confidence Interval Z-test

Density	5°	4°	3°	2°	Edge Slope	5°	4°	3°	2°
128	>=0.4	>=0.4	>=0.5	>=0.5	128	>=0.4	>=0.3	>=0.3	>=0.3
192	>=0.3	>=0.3	>=0.4	>=0.4	192	>=0.3	>=0.3	>=0.3	>=0.3
256	>=0.3	>=0.3	>=0.4	>=0.4	256	>=0.3	>=0.3	>=0.3	>=0.3
320	>=0.3	>=0.3	>=0.3	>=0.3	320	>=0.3	>=0.3	>=0.3	>=0.3
384	>=0.3	>=0.3	>=0.3	>=0.3	384	>=0.3	>=0.3	>=0.3	>=0.3
448	>=0.2	>=0.2	>=0.3	>=0.3	448	>=0.3	>=0.3	>=0.3	>=0.3
512	>=0.3	>=0.3	>=0.3	>=0.3	512	>=0.3	>=0.3	>=0.3	>=0.3

Using the same confidence interval, both the 'iradon' and the alternative reconstruction method are not statistically similar to the original image for density but do show similarity for edge definition as defined by edge slope. The optimization of pixel radius follows a pattern of being bimodal distributed for most image sizes and measured parameters. The parameters and overall optima group into either the minimum stable radius of 0.5 pixel or to the maximal tested at 1.0 pixel. Overall, the general trend is that 0.5 pixels would be the universally applicable radius.

Density values tend to be approaching the true value when the reconstruction stabilizes at 0.5 pixels radius. This fact holds true on all phantoms which is interesting considering the large difference in "structure" size between the "Shepp-Logan" and the Noise phantom. The "Shepp-Logan" phantom's eroded structure size is almost always greater than a 3x3 pixel square while the Noise phantom's eroded structure size is never above a single pixel unless you have overlapping 3x3 pixel diamonds of the same density. Using a 99.5% confidence interval Z-test to compare the "Shepp-Logan" at 1.0 pixel radius to the 0.5 pixel radius, the test failed to reject the null hypothesis that the two reconstructions are from the same population. This implies that while the numeric optimization might indicate optima at radii other than 0.5 pixel, there is no statistical difference between the results of using the 0.5 pixel optima.

Edge slope values similarly stabilize at 0.5 pixels radius for all but the "Shepp-Logan" phantom. The "Shepp-Logan" image differs significantly from the Ring phantom in that it has a larger number of edges between regions of relatively close density values while

the Ring phantom is largely structure on background edges. The Noise phantom has more edges that are between regions of relatively close density and also shows a tendency towards large circle radii for optimums. However with the Noise phantom, the small structure size causes density error to be the dominant term driving an overall optimum of 0.5 pixel radius.

For the oversized images, the edge slope is consistently optimized at 0.5 pixels radius however the density optima is more variable and occasionally becoming the dominant term driving the optima, especially for the "Shepp-Logan" phantom. As these images are more representative of real scans, the overall trend towards a 0.5 pixel radius optimum with in these images reinforces the general statement of 0.5 pixels being the most universal optima for all image and rotational step sizes. Of note is that the radius of a circle which has an area of 1 is 0.564 pixels, which is very close to the optimum found in the study.

CONCLUSION

Because the technique at any circle radius does not offer significant improvements over the linear interpolation method and is more computationally complex, it is not well suited to commercial application in the current form. There are significant improvements in the image quality at higher initial image sizes but no improvements numerically of the "3rd order" circle area technique over linear interpolation. This study utilized only the most basic Fourier filtering and further research could be done to optimize the filter and Nyquist frequency for reduction of the ray like artifacts in the image. These artifacts could potentially be a major source of the variations in the density and consequently edge slope data. Further work could be done on a larger cross-section of scans using radii between 0.4 and 0.6 pixels at finer spacing to further narrow in on an optima. Using images with larger ranges, smaller details or other metrics would validate the applicability of the optima to images across the spectrum of CT imaging.

REFFERENCES

Beckman, E. C. (2006). CT scanning the early days. *The British Journal of Radiography, Vol 79* , 5-8.

Buzug, T. M. (2008). *Computed Tomography: from photon statistics to modern cone beam CT*. Berlin: Springer.

GE Healthcare. (2008, January 25). *CT Definitions.* Retrieved May 19, 2011, from GE Healthcare-Education: www.gehealthcare.com/usen/education/tip.../CT%20Definitions.pdf

Goldman, L. W. (2007). Principles of CT and CT Technology. *Journal of Nuclear Medicine Technology, Vol 35* , 115-128.

Jackson, S. A. (2005). *Theory of Tomography.* Retrieved April 4, 2011, from radiologyphysics.bitica.com: http://www.radiologyphysics.bitica.com/files/Microsoft%20PowerPoint%20-%20Theory%20of%20Tomography.ppt.pdf

Lewitt, R. M., Bates, R. H., & Peters, T. M. (1978). Image Reconstruction from Projections II. Modified backprojection methods. *Optik* , 50-85.

Mathworks, Inc. (2004). iradon function. Natick, MA, USA.

Pendelton, B. (1992). *line3d - 3D Bresenham's (a 3D line drawing algorithm)*. Retrieved from ftp://ftp.isc.org/pub/usenet/comp.sources.unix/volume26/line3d.

Peters, T. M. (1981). Algorithms for Fast Back- and Re-projection in Computed Tomography. *IEEE, Transactions on Nuclear Science, Vol 28* , 3641-3647.

Ramachandran, G. N., & Lakshminarayanan, A. V. (1971). Three-dimensional Reconstruction from Radiographs and Electron. *Proc. Nat. Acad. Sci. USA, Vol 68* , 2236-2240.

Ruegesegger, e. a. (1980). Approximation of pixel area by a circle. *Oral Communication* . Swiss Federal Institute of Technology, Zurich, Switzerland.

Shepp, L. A., & Logan, B. F. (1974). RECONSTRUCTING HEAD TISSUE FROM X-RAY TRANSMISSIONS. *IEEE Transactions on Nuclear Science, Vol 21* , 228-236.

The Nobel Assembly of Karolinska Institutet. (1979, October 11). *Physiology or Medicine 1979 - Press Release*. Retrieved May 23, 2001, from http://nobelprize.org/nobel_prizes/medicine/laureates/1979/press.html RELATED DOCUMENTS: